www.sciencemag.org/cgi/content/full/339/6124/1198/DC1

Supplementary Materials for

A Reconstruction of Regional and Global Temperature for the Past 11,300 Years

Shaun A. Marcott,* Jeremy D. Shakun, Peter U. Clark, Alan C. Mix

*Corresponding author. E-mail: marcotts@science.oregonstate.edu

Published 8 March 2013, *Science* **339**, 1198 (2013)
DOI: 10.1126/science.1228026

This PDF file includes:

Supplementary Text
Figs. S1 to S26
Table S1
References

Other Supplementary Material for this manuscript includes the following:
(available at www.sciencemag.org/cgi/content/full/339/6124/1198/DC1)

Database S1

SUPPLEMENTAL MATERIALS

Marcott, S.A., Shakun, J.D., Clark, P.U., and Mix, A.C., *submitted 2012*, A Reconstruction of Regional and Global Temperature for the last 11,300 Years.

1. Database

This study is based on the following data selection criteria:

1. Sampling resolution is typically better than ~300 yr.
2. At least four age-control points span or closely bracket the full measured interval. Chronological control is derived from the site itself and not primarily based on tuning to other sites. Layer counting is permitted if annual resolution is plausibly confirmed (e.g., ice-core chronologies). Core tops are assumed to be 1950 AD unless otherwise indicated in original publication.
3. Each time series spans greater than 6500 years in duration and spans the entire 4500 – 5500 yr B.P. reference period.
4. Established, quantitative temperature proxies.
5. Data are publicly available (PANGAEA, NOAA-Paleoclimate) or were provided directly by the original authors in non-proprietary form.
6. All datasets included the original sampling depth and proxy measurement for complete error analysis and for consistent calibration of age models (Calib 6.0.1 using INTCAL09 (*1*)).

This study includes 73 records derived from multiple paleoclimate archives and temperature proxies (**Fig. S1; Table S1**): alkenone (n=31), planktonic foraminifera Mg/Ca (n=19), TEX_{86} (n=4), fossil chironomid transfer function (n=4), fossil pollen modern analog technique (MAT) (n=4), ice-core stable isotopes (n=5), other microfossil assemblages (MAT and Transfer Function) (n=5), and Methylation index of Branched Tetraethers (MBT) (n=1). Age control is derived primarily from ^{14}C dating of organic material; other established methods including tephrochronology or annual layer counting were used where applicable.

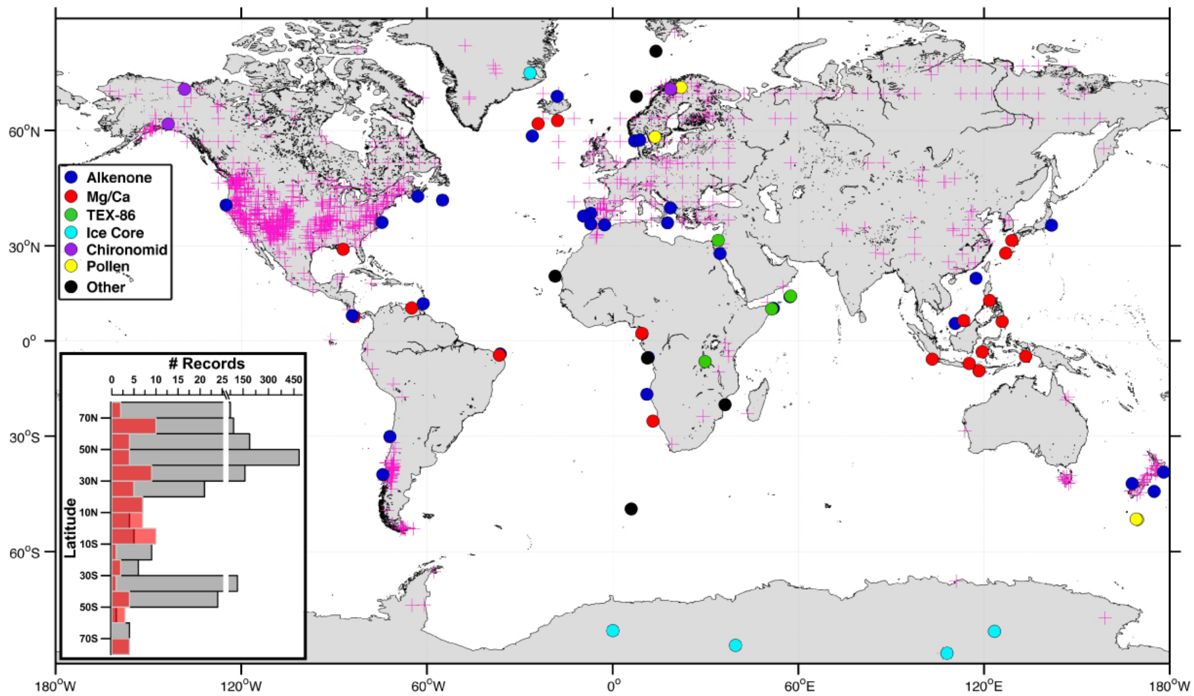

Fig. S1: Location map and latitudinal distribution of proxy temperature datasets. Map of temperature datasets from this study with temperature proxy identified by color coding (dots) and datasets used in Mann et al. (*2*) (crosses). (Inset) Latitudinal distribution of data from this study (red) and Mann et al. (*2*) (gray). Note break in y-axis at 25.

Table S1. List of data sets used in the global temperature stack.

Location / Core	Proxy	Temperature Calibration	Latitude (°)	Longitude (°)	Elevation (m a.s.l.)	Resolution (yr)	Published Seasonal Interpretation	Reference
GeoB5844-2	UK’37	Müller et al., 1998 (*3*)	27.7	34.7	-963	300	Annual / Summer	Arz et al., 2003 (*4*)
ODP-1019D	UK’37	Müller et al., 1998 (*3*)	41.7	-124.9	-980	140	Annual	Barron et al., 2003 (*5*)
SO136-GC11	UK’37	Müller et al., 1998 (*3*)	-43.5	167.9	-1556	290	Annual*	Barrows et al., 2007(*6*)
JR51GC-35	UK’37	Müller et al., 1998 (*3*)	67.0	-18.0	-420	110	Annual	Bendle and Rosell-Melé 2007 (*7*)
ME005A-43JC	Mg/Ca	Anand et al., 2003 (*8*)	7.9	-83.6	-1368	200	Annual*	Benway et al.,2006 (*9*)
MD95-2043	UK’37	Müller et al., 1998 (*3*)	36.1	-2.6	-1000	110	Annual	Cacho et al., 2001 (*10*)
M39-008	UK’37	Müller et al., 1998 (*3*)	39.4	-7.1	-576	140	Annual	Cacho et al., 2001 (*10*)
MD95-2011	UK’37	Müller et al., 1998 (*3*)	67.0	7.6	-1048	60	Summer	Calvo et al., 2002 (*11*)
ODP 984	Mg/Ca	Anand et al., 2003 (*8*)	61.4	-24.1	-1648	110	Winter*	Came et al., 2007 (*12*)
GeoB 7702-3	TEX86	Kim et al., 2008 (*13*)	31.7	34.1	-562	210	Summer	Castañeda et al., 2010 (*14*)
Moose Lake	Chironomid transfer function	Global Avg. RMSEP	61.4	-143.6	437	50	Summer	Clegg et al., 2010 (*15*)
ODP 658C	Foram transfer function	±1.5°C uncertainty	20.8	-18.6	-2263	110	Winter and Summer**	deMenocal et al., 2000 (*16*)
Composite: MD95-2011; HM79-4	Radiolaria transfer function	±1.2°C uncertainty	67.0	7.6	-	90	Summer	Dolven et al., 2002 (*17*)
IOW225517	UK’37	Müller et al., 1998 (*3*)	57.7	7.1	-293	120	Spring to Winter	Emeis et al., 2003 (*18*)
IOW225514	UK’37	Müller et al., 1998 (*3*)	57.8	8.7	-420	70	Spring to Winter	Emeis et al., 2003 (*18*)
M25/4-KL11	UK’37	Müller et al., 1998 (*3*)	36.7	17.7	-3376	260	Spring to Winter	Emeis et al., 2003 (*18*)
ODP 1084B	Mg/Ca	Mashiotta et al. 1999 (*19*)	-25.5	13.0	-1992	90	Winter	Farmer et al., 2005 (*20*)
AD91-17	UK’37	Müller et al., 1998 (*3*)	40.9	18.6	-844	190	Annual (seasonal bias likely)	Giunta et al., 2001 (*21*)
74KL	UK’37	Müller et al., 1998 (*3*)	14.3	57.3	-3212	300	Annual (seasonal bias likely)	Huguet et al., 2006 (*22*)
74KL	TEX86	Schouten et al., 2002 (*23*)	14.3	57.3	-3212	300	Annual (seasonal bias likely)	Huguet et al., 2006 (*22*)
NIOP-905	UK’37	Müller et al., 1998 (*3*)	10.6	51.9	-1567	180	Annual (seasonal bias likely)	Huguet et al., 2006 (*22*)
NIOP-905	TEX86	Schouten et al., 2002 (*23*)	10.6	51.9	-1567	180	Annual (seasonal bias likely)	Huguet et al., 2006 (*22*)
Composite: MD01-2421; KR02-06 St.A GC; KR02-06 St.A MC	UK’37	Müller et al., 1998 (*3*)	36.0	141.8	-2224	60	Annual*	Isono et al., 2009 (*24*)

GeoB 3910	UK'37	Müller et al., 1998 (*3*)	-4.2	-36.3	-2362	400	Annual*	Jaeschke et al., 2007 (*25*)
Dome C, Antarctica	Ice Core δD	±30% uncertainty	-75.1	123.4	3240	20	Annual	Jouzel et al., 2007 (*26*)
GeoB 7139-2	UK'37	Müller et al., 1998 (*3*)	-30.2	-72.0	-3270	500	Annual	Kaiser et al., 2008 (*27*)
Dome F, Antarctica	Ice Core $\delta^{18}O$, δD	±30% uncertainty	-77.3	39.7	3810	500	Annual	Kawamura et al., 2007 (*28*)
18287-3	UK'37	Müller et al., 1998 (*3*)	5.7	110.7	-598	260	Annual	Kienast et al., 2001 (*29*)
GeoB 1023-5	UK'37	Müller et al., 1998 (*3*)	-17.2	11.0	-1978	180	Annual	Kim et al., 2002 (*30*)
GeoB 5901-2	UK'37	Müller et al., 1998 (*3*)	36.4	-7.1	-574	120	Annual	Kim et al., 2004 (*31*)
KY07-04-01	Mg/Ca	Anand et al., 2003 (*8*)	31.6	129.0	-2114	100	Summer	Kubota et al., 2010 (*32*)
Hanging Lake	Chironomid transfer function	Global Avg. RMSEP	68.4	-138.4	500	150	Summer	Kurek et al., 2009 (*33*)
GeoB 3313-1	UK'37	Müller et al., 1998 (*3*)	-41.0	-74.3	825	90	Annual	Lamy et al., 2002 (*34*)
Lake 850	Chironomid transfer function	Global Avg. RMSEP	68.4	19.2	850	80	Summer	Larocque et al., 2004 (*35*)
Lake Nujulla	Chironomid transfer function	Global Avg. RMSEP	68.4	18.7	999	190	Summer	Larocque et al., 2004 (*35*)
PL07-39PC	Mg/Ca	Anand et al., 2003 (*8*)	10.7	-65.0	-790	180	Annual	Lea et al., 2003 (*36*)
MD02-2529	UK'37	Müller et al., 1998 (*3*)	8.2	-84.1	-1619	290	Summer*	Leduc et al., 2007 (*37*)
MD98-2165	Mg/Ca	Dekens et al., 2002 (*38*)	-9.7	118.3	-2100	220	Annual	Levi et al., 2007 (*39*)
MD79-257	Foram MAT	±1.1°C uncertainty	-20.4	36.3	-1262	300	Winter and Summer**	Levi et al., 2008 (*39*)
BJ8 13GGC	Mg/Ca	Anand et al., 2003 (*8*)	-7.4	115.2	-594	40	Annual*	Linsley et al., 2010 (*40*)
BJ8 70GGC	Mg/Ca	Anand et al., 2003 (*8*)	-3.6	119.4	-482	130	Annual*	Linsley et al., 2011 (*40*)
MD95-2015	UK'37	Müller et al., 1998 (*3*)	58.8	-26.0	-2630	80	Annual	Marchal et al., 2002 (*41*)
Homestead Scarp	Pollen MAT	±0.98°C uncertainty	-52.5	169.1	30	70	Summer	McGlone et al., 2010 (*42*)
Mount Honey	Pollen MAT	±0.98°C uncertainty	-52.5	169.1	120	110	Summer	McGlone et al., 2011 (*42*)
GeoB 10038-4	Mg/Ca	Anand et al., 2003 (*8*)	-5.9	103.3	-1819	530	Annual	Mohtadi et al., 2010 (*43*)
TN05-17	Diatom MAT	±0.75°C uncertainty	-50.0	6.0	-3700	40	Annual**	Nielsen et al., 2004 (*44*)
MD97-2120	UK'37	Müller et al., 1998 (*3*)	-45.5	174.9	-3290	160	Annual	Pahnke and Sachs, 2005 (*45*)
MD97-2121	UK'37	Müller et al., 1998 (*3*)	-40.4	178.0	-3014	80	Annual	Pahnke and Sachs, 2006 (*45*)
17940	UK'37	Müller et al., 1998 (*3*)	20.1	117.4	-1968	120	Annual	Pelejero et al., 1999 (*46*)
Vostok, Antarctica	Ice Core δD	±30% uncertainty	-78.5	108.0	3500	40	Annual*	Petit et al., 1999 (*47*)
D13822	UK'37	Müller et al., 1998 (*3*)	38.6	-9.5	-88	70	Summer*	Rodriguez et al., 2009 (*48*)
M35003-4	UK'37	Müller et al., 1998 (*3*)	12.1	-61.2	-1299	290	Annual	Rühlemann et al., 1999 (*49*)

OCE326-GGC26	UK'37	Müller et al., 1998 (*3*)	43.0	-55.0	-3975	110	Annual	Sachs 2007 (*50*)
OCE326-GGC30	UK'37	Müller et al., 1998 (*3*)	44.0	-63.0	-250	80	Annual	Sachs 2007 (*50*)
CH07-98-GGC19	UK'37	Müller et al., 1998 (*3*)	36.9	-74.6	-1049	60	Annual	Sachs 2007 (*50*)
GIK23258-2	Foram transfer function	±1.5°C uncertainty	75.0	14.0	-1768	40	Winter and Summer**	Sarnthein et al., 2003 (*51*)
GeoB 6518-1	UK'37	Müller et al., 1998 (*3*)	-5.6	11.2	-962	180	Annual*	Schefuß et al., 2005 (*52*)
Flarken Lake	Pollen MAT	Seppa et al., 2005 (*53*)	58.6	13.7	108	100	Annual	Seppä and Birk, 2001; Seppä et al. 2005 (*53, 54*)
Tsuolbmajavri Lake	Pollen MAT	Seppa et al., 2005 (*53*)	68.7	22.1	526	70	Summer	Seppä and Birk, 2001; Seppä et al 1999 (*54, 55*)
MD01-2390	Mg/Ca	Dekens et al., 2002 (*38*)	6.6	113.4	-1545	200	Annual (wt. toward summer)	Steinke et al., 2008 (*56*)
EDML	Ice Core $\delta^{18}O$	±30% uncertainty	-75.0	0.1	2892	100	Annual*	Stenni et al., 2010 (*57*)
MD98-2176	Mg/Ca	Anand et al., 2003 (*8*)	-5.0	133.4	-2382	60	Annual*	Stott et al., 2007 (*58*)
MD98-2181	Mg/Ca	Anand et al., 2003 (*8*)	6.3	125.8	-2114	50	Annual*	Stott et al., 2007 (*58*)
A7	Mg/Ca	Anand et al., 2003 (*8*)	27.8	127.0	-1262	110	Late Spring to Summer	Sun et al., 2005 (*59*)
RAPID-12-1K	Mg/Ca	Thornalley et al., 2009 (*60*)	62.1	-17.8	-1938	80	Late Spring to early Summer	Thornalley et al., 2009 (*60*)
NP04-KH3, -KH4	TEX86	Powers et al., 2005 (*61*)	-6.7	29.8	773	190	Annual*	Tierney et al., 2008 (*62*)
Agassiz & Renland	Ice Core $\delta^{18}O$, borehole temp.	±30% uncertainty	71.3/ 81.0	26.7 / -71	1730 & 2350	20	Annual*	Vinther et al., 2009 (*63*)
GeoB6518-1	MBT	±0.2°C uncertainty	-5.6	11.2	-962	140	Annual	Weijers et al., 2007 (*64*)
MD03-2707	Mg/Ca	Dekens et al., 2002 (*38*)	2.5	9.4	-1295	40	Annual*	Weldeab et al., 2007 (*65*)
GeoB 3129	Mg/Ca	Anand et al., 2003 (*8*)	-4.6	-36.6	-830	160	Annual*	Weldeab et al., 2006 (*66*)
GeoB 4905	Mg/Ca	Anand et al., 2003 (*8*)	2.5	9.4	-1328	250	Annual*	Weldeab et al., 2005 (*67*)
MD01-2378	Mg/Ca	Anand et al., 2003 (*8*)	13.1	121.8	-1783	130	Annual*	Xu et al., 2008 (*68*)
MD02-2575	Mg/Ca	Anand et al., 2003 (*8*)	29.0	-87.1	-847	250	Summer	Ziegler et al., 2008 (*69*)

* Seasonal interpretation not explicitly stated, but inferred based on comparison of core-top proxy measurement to annual/seasonal instrumental temperature at site or inferred from general discussion in the text.
**Both winter and summer reconstructions were provided and were averaged together; assumed to represent annual average temperature

2. Uncertainty

We consider two sources of uncertainty in the paleoclimate data: proxy-to-temperature calibration (which is generally larger than proxy analytical reproducibility) and age uncertainty. We combined both types of uncertainty while generating 1000 Monte Carlo realizations of each record.

Proxy temperature calibrations were varied in normal distributions defined by their 1σ uncertainty. Added noise was not autocorrelated either temporally or spatially.

a. Mg/Ca from Planktonic Foraminifera – The form of the Mg/Ca-based temperature proxy is either exponential or linear:

$$Mg/Ca = (B \pm b)*\exp((A \pm a)*T)$$

$$Mg/Ca = (B \pm b)*T - (A \pm a)$$

where *T*=temperature.

For each Mg/Ca record we applied the calibration that was used by the original authors. The uncertainty was added to the "A" and "B" coefficients (1σ "a" and "b") following a random draw from a normal distribution.

b. $U^{K'}_{37}$ from Alkenones – We applied the calibration of Müller et al. (*3*) and its uncertainties of slope and intercept.

$$U^{K'}_{37} = T*(0.033 \pm 0.0001) + (0.044 \pm 0.016)$$

c. TEX_{86} – We applied the calibration suggested by the original authors and the uncertainty from the global core top calibration of Kim et al. (*13*) (± 1.7°C, 1σ).

d. Chironomids – We used the average root mean squared error (± 1.7°C, 1σ) from six studies (*70-75*) and treated it as the 1σ uncertainty for all of the temperature measurements.

e. Pollen – The uncertainty follows Seppä et al. (*53*) (± 1.0°C) and was treated as 1σ.

f. Ice core – We conservatively assumed an uncertainty of ±30% of the temperature anomaly (1σ).

g. All other methods – The uncertainty for the remaining records was derived from the original publications (**Table S1**) and treated as the 1σ temperature uncertainty.

The majority of our age-control points are based on radiocarbon dates. In order to compare the records appropriately, we recalibrated all radiocarbon dates with Calib 6.0.1 using INTCAL09 and its protocol (*1*) for the site-specific locations and materials. Any reservoir ages used in the ocean datasets followed the original authors' suggested values, and were held constant unless otherwise stated in the original publication. To account for age uncertainty, our Monte Carlo procedure perturbed the age-control points within their uncertainties. The uncertainty between the age-control points was modeled as a random walk (*76*), with a "jitter" value of 150 (*77*). Chronologic uncertainty was modeled as a first-order autoregressive process with a coefficient of 0.999. For the layer-counted ice-core records, we applied a ±2% uncertainty for the Antarctic sites and a ±1% uncertainty for the Greenland site (1σ).

3. Monte-Carlo-Based Procedure

We used a Monte-Carlo-based procedure to construct 1000 realizations of our global temperature stack. This procedure was done in several steps:

1) We perturbed the proxy temperatures for each of the 73 datasets 1000 times (see Section 2) (**Fig. S2a**).

2) We then perturbed the age models for each of the 73 records (see Section 2), also 1000 times (**Fig. S2a**).

3) The first of the perturbed temperature records was then linearly interpolated onto the first of the perturbed age-models at 20 year resolution, and this was continued sequentially to form 1000 realizations of each time series that incorporated both temperature and age uncertainties (**Fig. S2a**). While the median resolution of the 73 datasets is 120 years, coarser time steps yield essentially identical results (see below), likely because age-model uncertainties are generally larger than the time step, and so effectively smooth high-frequency variability in the Monte Carlo simulations. We chose a 20-year time step in part to facilitate comparison with the high-resolution temperature reconstructions of the past millennium.

4) The records were then converted into anomalies from the average temperature for 4500-5500 yrs BP in each record, which is the common period of overlap for all records.

5) The records were then stacked together by averaging the first realization of each of the 73 records, and then the second realization of each, then the third, the fourth, and so on to form 1000 realizations of the global temperature stack (**Fig.S2 b,c and Fig. S3)**.

6) The mean temperature and standard deviation were then taken from the 1000 simulations of the global temperature stack (**Fig. S2d**), and aligned with Mann et al. (2) over the interval 510-1450 yr BP (i.e. 500-1440 AD/CE), adjusting the mean, but not the variance. Mann et al. (2) reported anomalies relative to the CE 1961-1990 average; our final reconstructions are therefore effectively anomalies relative to same reference interval.

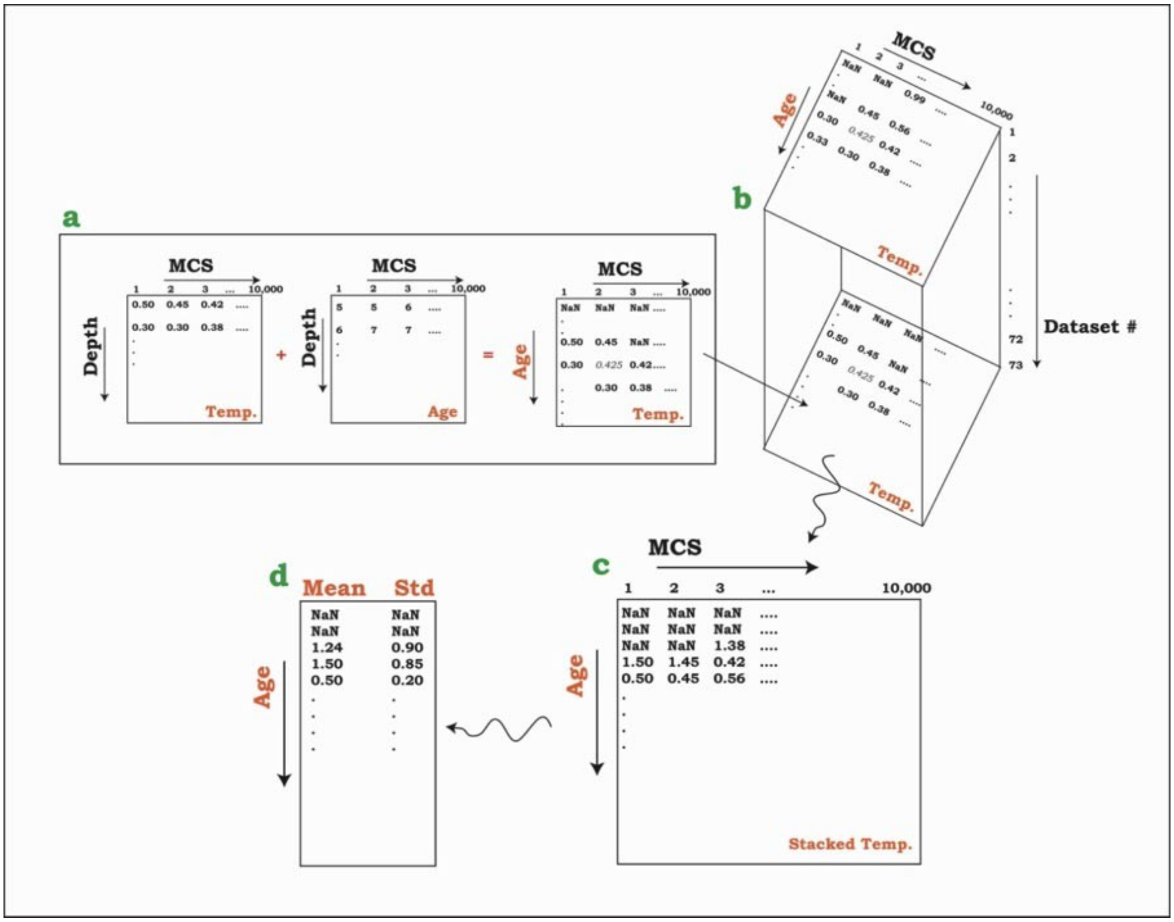

Fig. S2: Monte Carlo procedure. **(a)** Combining perturbed temperature (Temp.) and age model values to form 1000 simulated versions of each dataset (labeled 10,000 in this diagram). **(b)** Three dimensional matrix of each of the 1000 simulated datasets. **(c)** 1000 realizations of the globally stacked temperature record after averaging the datasets. **(d)** Mean and standard deviation (Std) of the 1000 globally stacked temperature records. MCS – Monte Carlo Simulations.

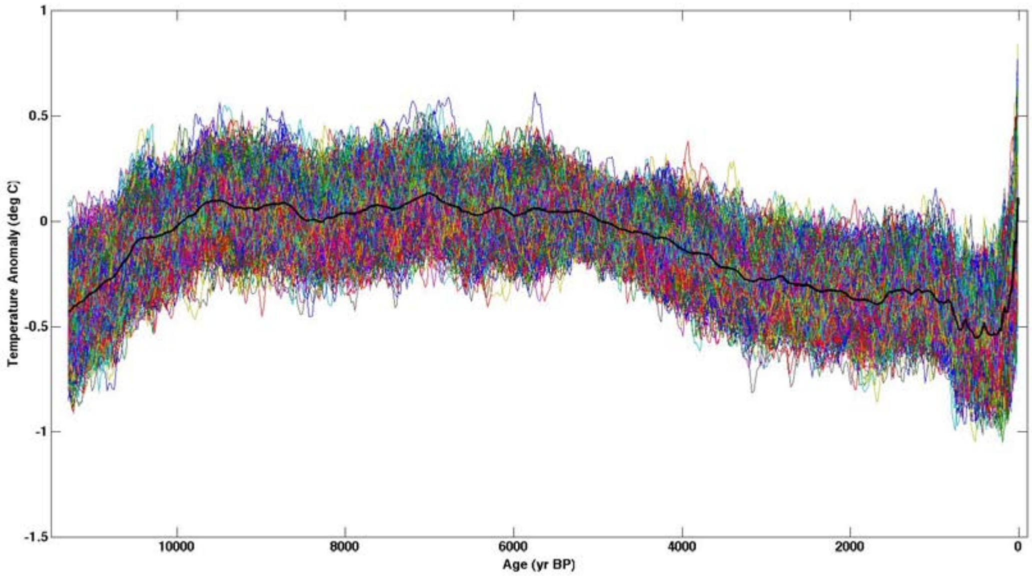

Fig. S3: 1000 realizations of the globally stacked time series (colored lines) and the mean (black line). Temperature anomaly is relative to the 4500-5500 yr B.P. mean. The realizations were derived using the Standard method (see below).

4. Construction of Stacks

We constructed the temperature stack using several different weighting schemes to test the sensitivity of the temperature reconstruction to spatial biases in the dataset. These include an arithmetic mean of the datasets (Standard method), both an area-weighted 5°x5° and 30°x30° lat-lon gridded average, a 10° latitudinal area-weighted mean, and a calculation of 1000 jackknifed stacks that randomly exclude 30% and 50% of the records in each realization (**Fig. S4 and S8**). We also used a data infilling method based on a regularized expectation maximization algorithm (RegEM; default settings) (*78*). The uncertainty envelope we report for RegEM combines the Monte Carlo simulation uncertainty with that provided by the RegEM code (*78*).

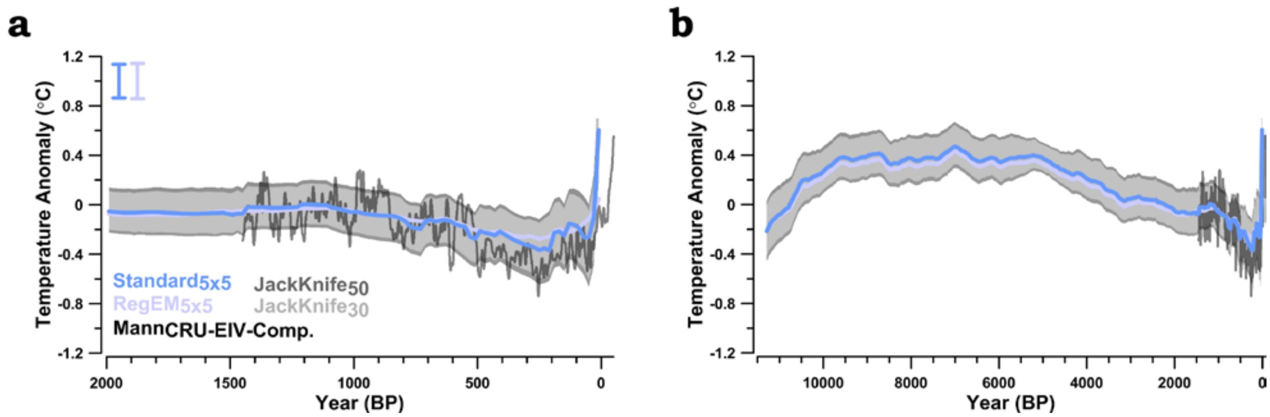

Fig. S4: Temperature reconstructions separated by method. **(a)** 5x5 degree weighted temperature envelope (1-σ) of the jack-knifed global temperature anomaly (30% removed light gray fill; 50% removed dark gray fill), RegEM infilled anomaly (light purple line), standard temperature anomaly (blue line) and Mann et al.'s(*2*) global temperature CRU-EIV composite (darkest gray). Uncertainty bars in upper left corner reflect the average Monte Carlo based 1σ uncertainty for each reconstruction, and were not overlain on line for clarity. **b** same as **a but** for the last 11,300 years. Temperature anomaly is from the CE 1961-1990 average.

5. Seasonal Proxy Bias

Some paleoclimate proxy data may be biased toward a specific season (*79, 80*). To test for such effects in the stack, we compared different temperature proxies that were either collected from the same site or from sites that are within 5°of latitude or longitude of each other (**Fig. S5 and S6**). Given the chronologic and calibration uncertainties estimated with our Monte Carlo simulations, we do not find a significant temperature difference between unlike proxies within 5° of each other. We further assess whether a bias exists by taking the difference in temperature between all unlike proxies from the same site (i.e., within 5° of latitude or longitude), and taking the difference in temperature between all like proxies from the same site. In the first case, based on 10 such pairs, the difference is 1.6 ± 1.0°C (1σ), which is similar to the average difference between records based on the same proxy 2.1 ± 1.0°C (1σ) (**Fig. S7**). These results suggest that if a seasonal bias exists between proxies, it adds no more uncertainty than that associated with proxy-temperature calibrations.

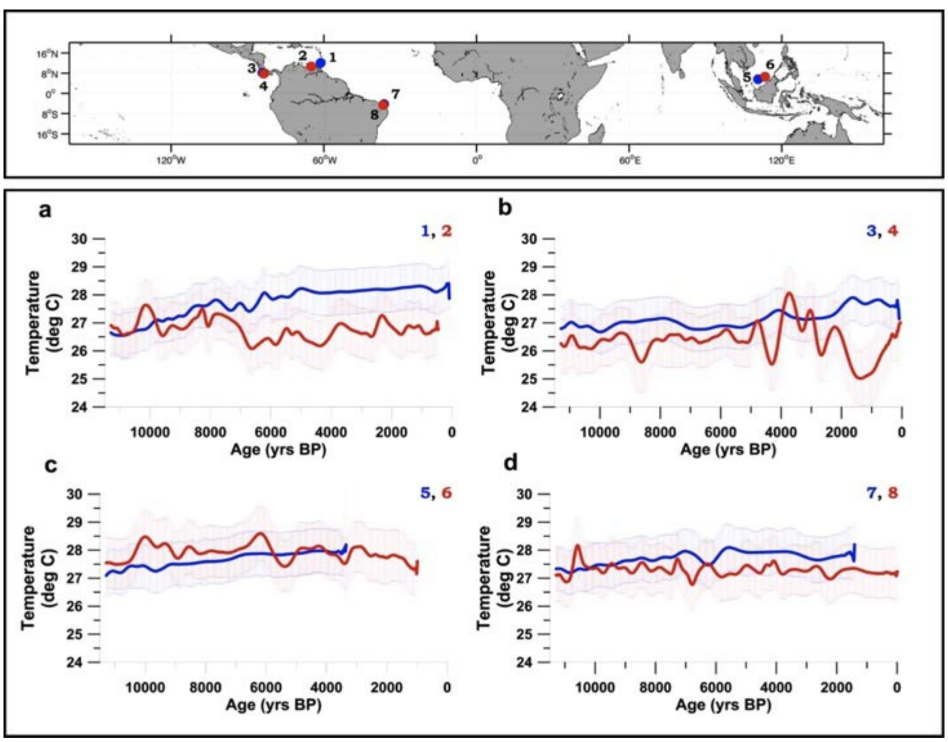

Fig. S5: Upper. Map showing location of sites. **Lower.** Temperature reconstructions at select sites where different proxy-based reconstructions were used. In each of these comparisons, the blue lines represent temperature reconstructions derived from alkenones ($U^{K'}_{37}$) and the red lines represent temperatures from planktonic foraminifera (Mg/Ca).

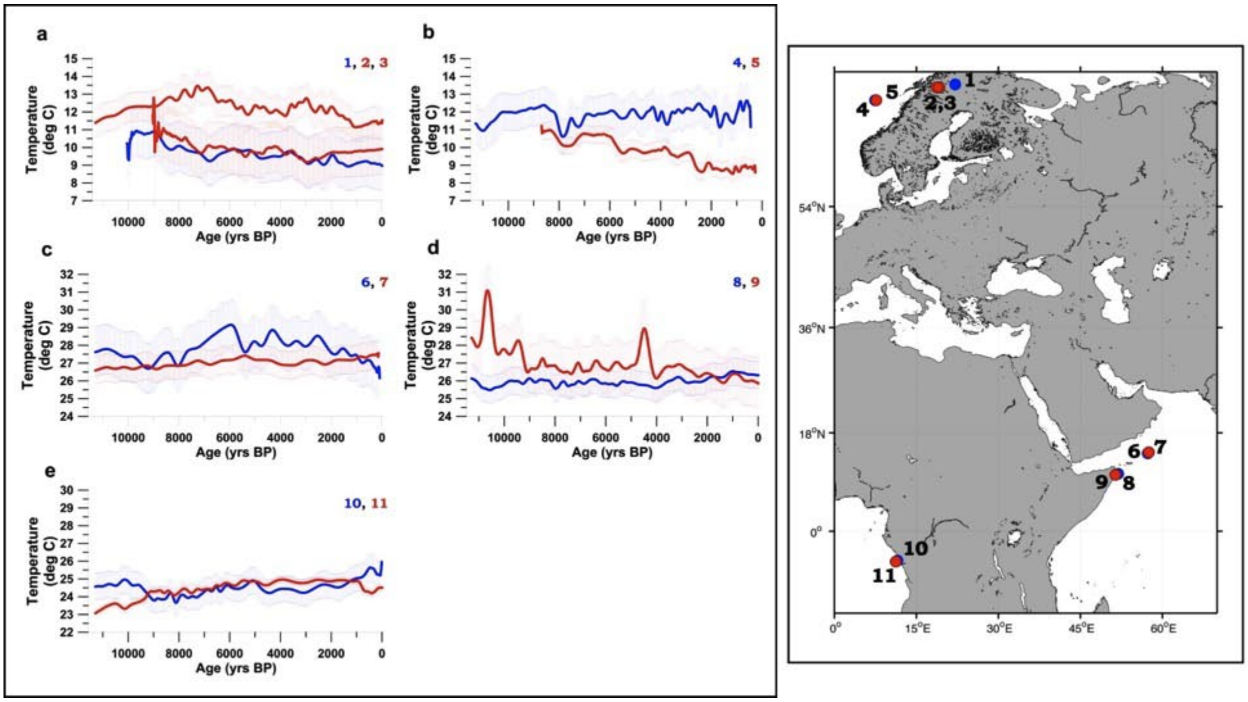

Fig. S6: Left. Temperature reconstructions at select sites where different proxy-based reconstructions were used. **(a)** Pollen temperature reconstruction (blue) compared with chironomid records (red). **(b)** Alkenone ($U^{K'}_{37}$) record (blue) compared with radiolaria record (red). **(c,d)** Alkenone records ($U^{K'}_{37}$) (blue) compared with TEX_{86} records (red). **(e)** Alkenone record ($U^{K'}_{37}$) (blue) compared with branched tetraether membrane lipid (MBT) record (red). **Right.** Map showing location of sites.

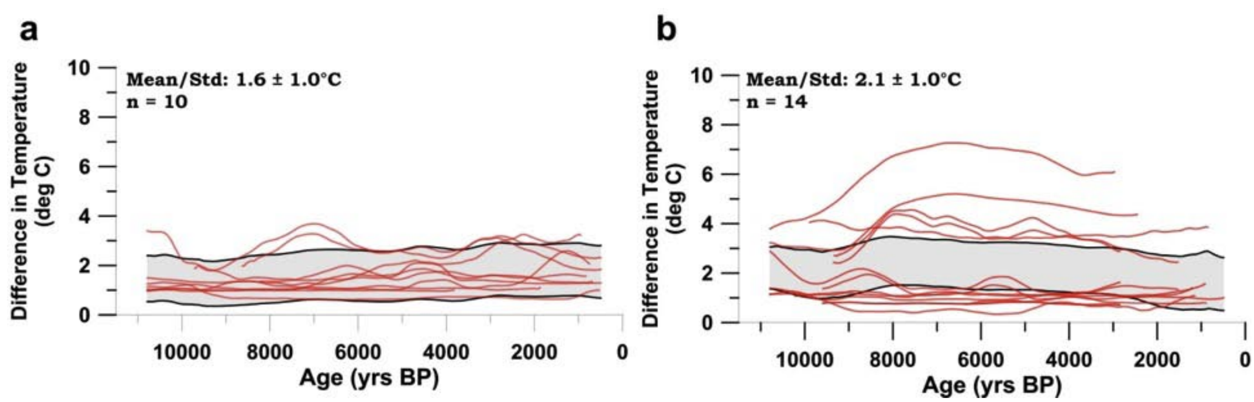

Fig. S7: Average absolute value of difference between pairs records that are found within 5°'s of latitude or longitude of each other. **(a)** Difference in absolute temperature through time for records using unlike proxy-based temperature methods (red lines) with the 1σ envelope for all ten differences (grey bar). **(b)** Same as (**a**) but for records using the same proxy-based temperature method.

We used published output from a transient simulation of the Holocene with the ECBilt-CLIO model (*81*) to test for potential impacts of seasonal proxy bias on the global temperature stack. We sampled the surface-air temperatures from the model at our proxy locations in the season of interest, assuming summer bias for Mg/Ca and alkenones at high northern latitudes and equatorial sites (*80*) and the bias suggested by the original authors for temperature reconstructions from other regions (Table S1). The results were then stacked into a global composite and compared to the mean-annual temperature from the model at the same locations (**Fig. S8**). The seasonally biased model stack tends to over represent an early Holocene warming in the modeled mean-annual temperature by 0.25°C, but the two stacks are otherwise quite similar. Inclusion of a wide variety of proxies with different potential seasonal biases likely helps to buffer the stacked record against such biases that may be unique to specific proxies or regions.

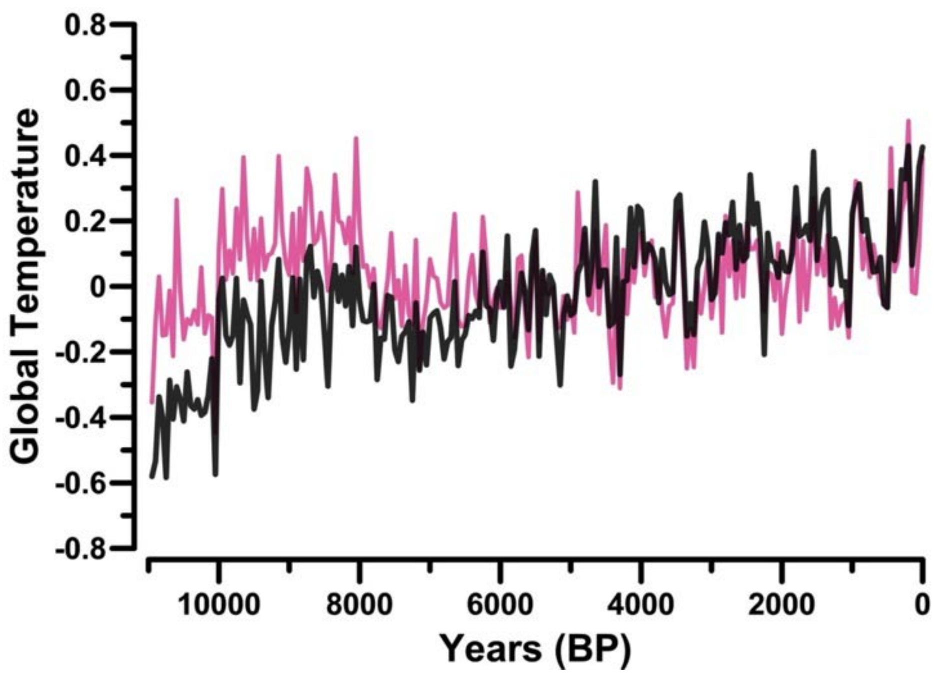

Fig. S8: Simulated global mean temperature for the last 11000 years at the 73 proxy sites (black) from the ECBilt-CLIO transient simulations (*81*), and the global mean temperature assuming a seasonal proxy bias (red) as described in text.

We compared all of the methods for deriving the temperature stack (**Fig. S9**) to a 5°x5° weighted stack ($Standard\_Publ_{5x5}$) that is derived from records that only represent annual average temperatures as suggested from the original publication (n=50) (**Table S1**). The $Standard\_Publ_{5x5}$ reconstruction has a higher amplitude of change than the $Standard_{5x5}$ reconstruction, but it retains the same long-term structure seen in the $Standard_{5x5}$ reconstruction, providing additional confidence that seasonal biases are minimal in this reconstruction.

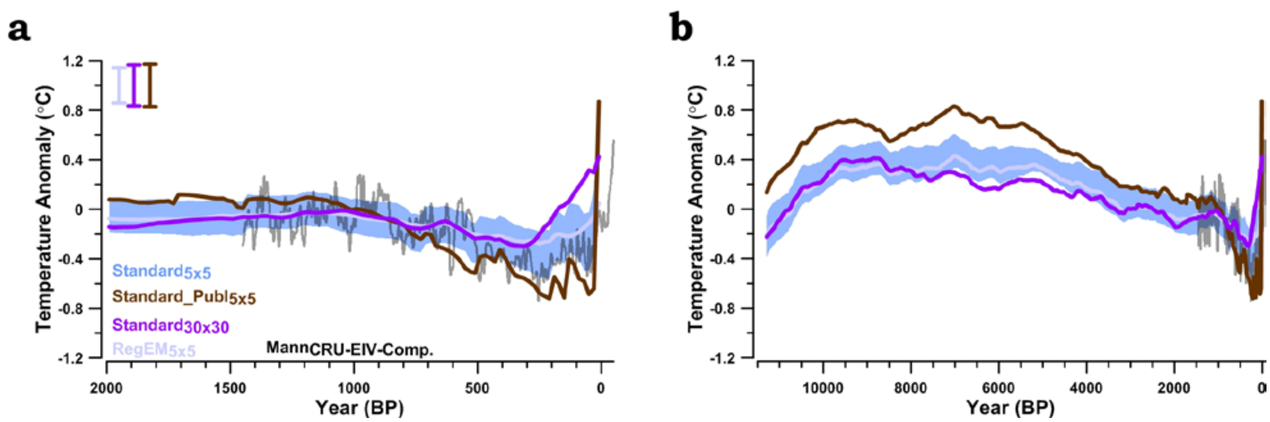

Fig. S9: Temperature reconstructions separated by method. **(a)** 5x5 degree weighted temperature envelope (1-σ) of the global temperature anomaly (blue fill), 30x30 degree weighted anomaly (purple line), RegEM infilled anomaly (light purple line), published annual anomaly (brown line) and Mann et al.'s (*2*) global temperature CRU-EIV composite (dark gray). Color uncertainty bars in upper left corner reflect the average Monte Carlo based 1σ uncertainty for each reconstruction. **b** same as **a** for the last 11,300 years. Temperature anomaly is from the CE 1961-1990 average.

6. Latitudinal, Terrestrial, and Ocean Reconstructions

Separate temperature stacks were constructed for 30° latitude bands, for different proxy types, and for land vs. ocean data. High latitudes changed more than low latitudes (**Fig. S10**). The bands 90-60°N, 60-30°N and 30-60°S are dominated by long-term cooling trends, while the bands 30-0°N, 0-30°S, and 60-90°S show little trend and are characterized primarily by millennial-scale variability.

The majority of the datasets that comprise our temperature stack come from sea-surface temperature reconstructions (n_{ocean} = 58 vs. n_{land} = 15). Ocean and land stacks (**Fig. S11c,f**) agree within uncertainty in spite of geographical biases (**Fig. S11a,d**). The spread among the resulting stacks is generally smaller than the long-term Holocene cooling trend.

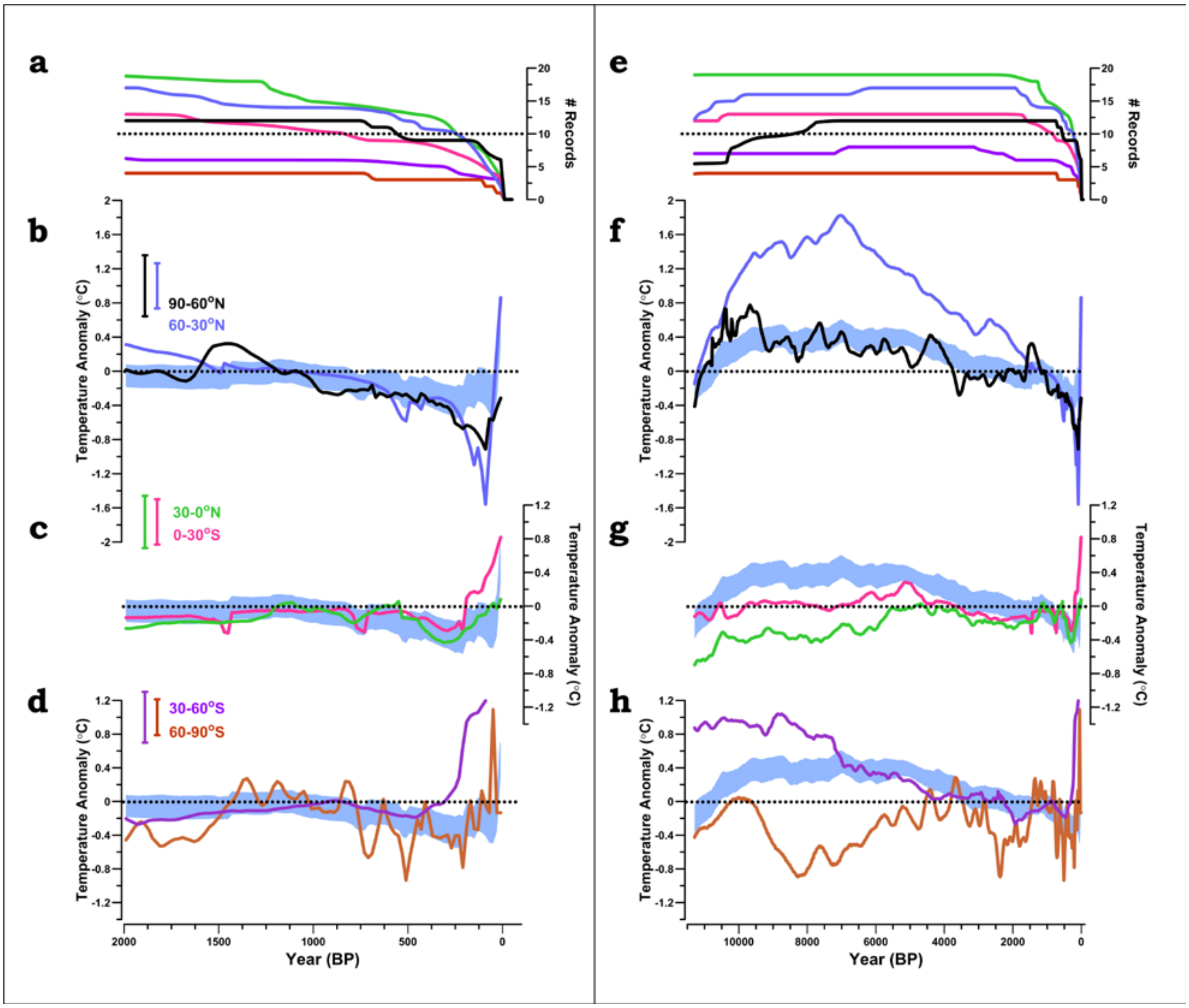

Fig. S10: Temperature reconstructions separated by latitude. **(a)** Number of records used to construct the temperature stack through time for the 5x5 degree weighted 90-60°N sites (**black** line), 60-30°N sites (blue line), 30-0°N sites (green line), 0-30°S sites (pink line), 30-60°S sites (purple line), and 60-90°S sites (brown line). **(b-d)** 5x5 degree weighted temperature envelope (1-σ) of the global temperature anomaly (blue fill) plotted against the 5x5 degree weighted latitudinal sites. Uncertainty bars in upper left corner reflect the average Monte Carlo based 1σ uncertainty for each reconstruction, and were not overlain on line for clarity. **e-h** same as **a** for the last 11,300 years. Temperature anomaly is from the CE 1961-1990 average. Note that **b** and **f** have larger y-axes, but are scaled the same as the axes in **c,d,g,h**.

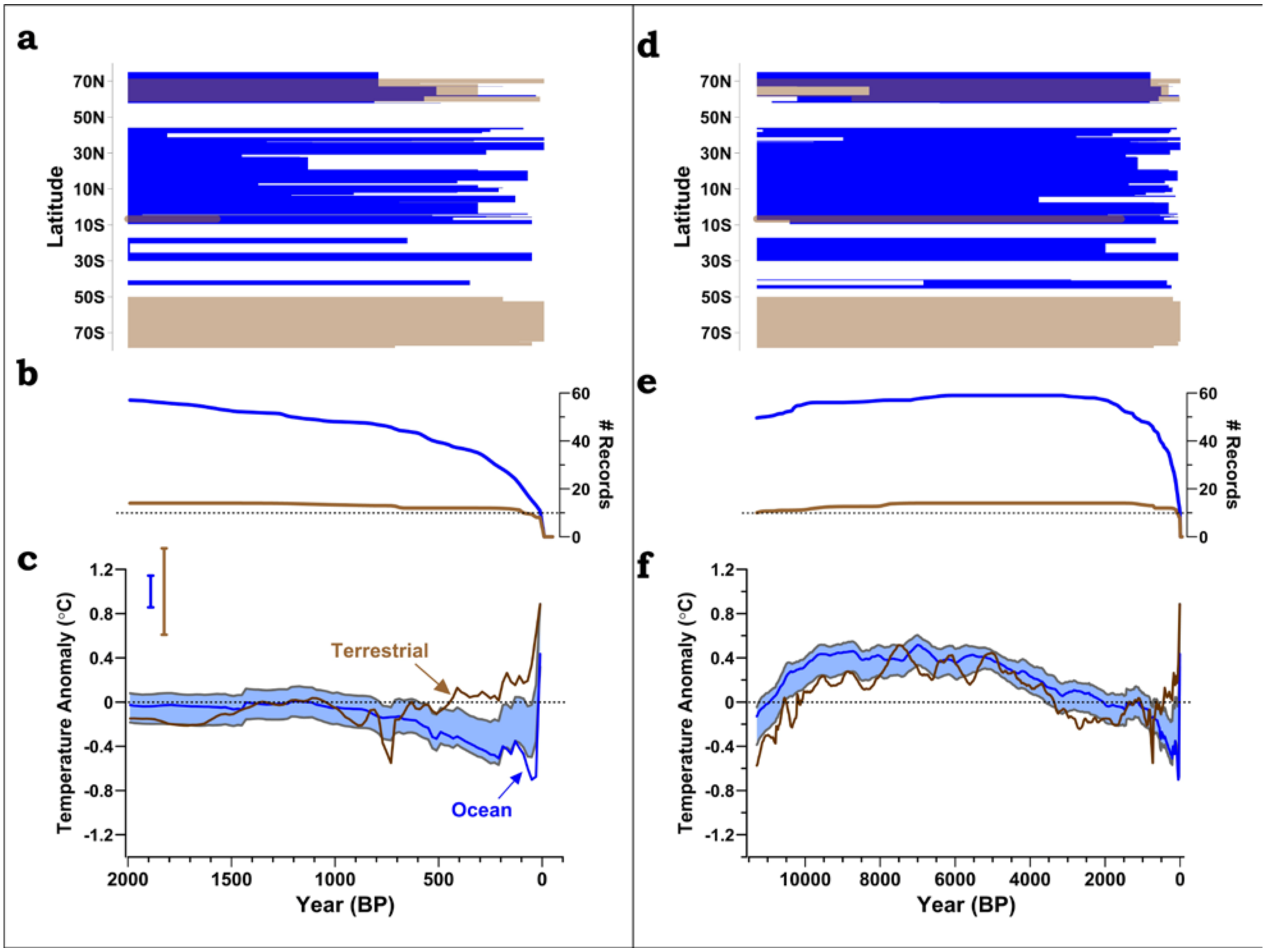

Fig. S11: Temperature reconstructions separated by ocean vs land. **(a)** Latitudinal distribution of the records used to construct the terrestrial (brown bars), and ocean records (blue bars). **(b)** Number of records used to construct the temperature stacks through time (terrestrial – brown line; ocean–blue line). **(c)** Global temperature anomaly 1-σ envelope (5x5 degree weighted) (blue fill) and terrestrial (brown), and ocean records (blue). Uncertainty bars in upper left corner reflect the average Monte Carlo based 1σ uncertainty for each reconstruction, and were not overlain in plot for clarity. **d-f** same as **a-c** for the last 11,300 years. Temperature anomaly is from the CE 1961-1990 average.

7. Sampling Resolution

One question regarding potential smoothing of our global temperature stack is what effect the choice of time-step (20 yrs) used in this study has on our results. The average sampling resolution of the datasets is 160 years, the median is 120 years, and the full range spans from 20 to 500 years (**Table S1**). We used the highest resolution time-step in order to preserve as much of the variability in the stack as possible. Because all of the datasets do not span the entirety of the Holocene and because the highest resolution datasets typically include the last 1500 years, the goal was to pick a resolution that could incorporate all of the variability with respect to time and not be limited by the coarser resolution data. However, in doing so, we interpolate between real data points, which could thus be inadvertently adding signal or an apparent oscillation that would otherwise not exist had we interpolated to a coarser resolution (i.e. aliasing (*82*)). To test the sensitivity of the time-step, we recalculated the global mean temperature using a 100- and 200-year resolution (**Fig. S12**). While some small differences occur between the reconstructions, they are well within the uncertainty of the global temperature stack and do not affect our conclusions and general interpretations for this study. This result is not particularly surprising as the Monte Carlo simulations themselves act to smooth the datasets and filter out any potential anomalous results based on the chosen time-step. The Monte Carlo procedure acts much like a Gaussian filter as it moves forward and backward in time (i.e. chronologic uncertainty) pinned to a central point that is defined by the age control points.

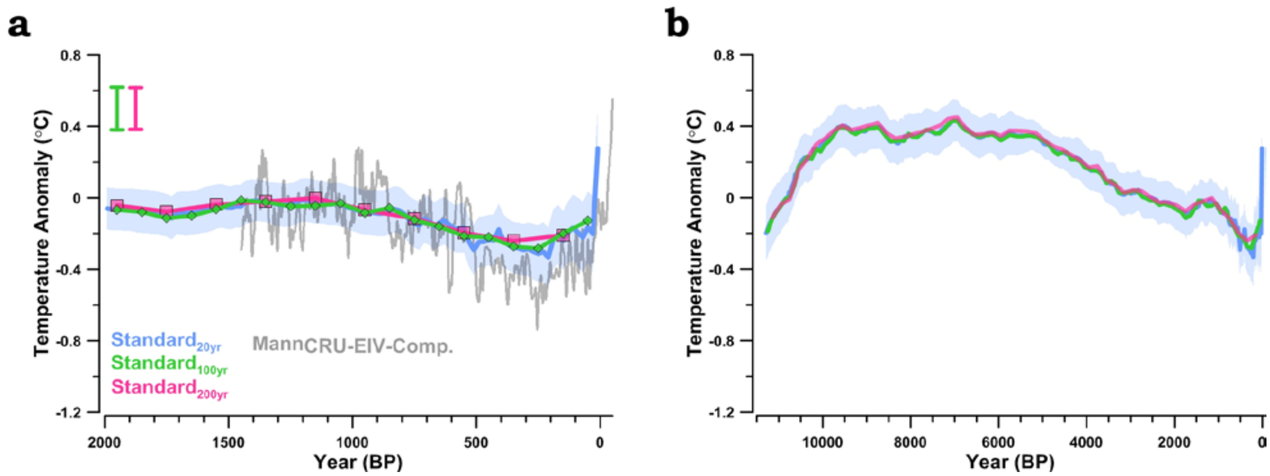

Fig. S12: Temperature reconstructions using multiple time-steps. **(a)** Global temperature envelope (1-σ) (light blue fill) and mean of the standard temperature anomaly using a 20 year interpolated time-step (blue line), 100 year time-step (pink line), and 200 year time-step (green line). Mann et al.'s (*2*) global temperature CRU-EIV composite (darkest gray) is also plotted. Uncertainty bars in upper left corner reflect the average Monte Carlo based 1σ uncertainty for each reconstruction, and were not overlain on line for clarity. **b** same as **a** for the last 11,300 years. Temperature anomaly is from the 1961-1990 yr B.P. average after mean shifting to Mann et al.(*2*).

8. Global Temperature Reconstruction from Sparse Dataset

To examine whether 73 locations accurately represent the average global temperature through time, we used the surface air temperature from the 1x1° grid boxes in the NCEP-NCAR reanalysis (*83*) from 1948-2008 as well as the NCDC land-ocean dataset from 1880-2010 (*84*). (**Fig. S13 and S14**). We then conducted three experiments. (1) We selected random grid points from the global temperature field, and analyzed these grid points for each year between 1948 and 2008. Grid points changed with each realization, but stayed constant through time for each realization. (2) We then repeated the experiment, but allowed the grid points to change with each realization as well as through time; this produces a very similar result as in step 1 (**Fig. S14**). After selecting ~25 data points the correlation between the subset time series and the full temperature time series from 1948-2008 is >0.80, and by 70 data points the correlation is greater than 0.90 (**Fig. S13)**. (3) We then selected data from the grid boxes where our proxy records occur. The average temperature anomaly at these proxy locations is very similar to the global mean (**Fig. S14**).

We next used the NCDC land-ocean data set, which spans a greater period of time than the NCEP-NCAR reanalysis. Comparison of the global temperature history for the last 130 years to the temperature history derived from the 73 locations of our data sites shows agreement within 0.1°C (**Fig. S15**). Finally, we used the modeled surface-air temperature from ECBilt-CLIO (*81*) in the same way as the NCDC land-ocean data set, and again find agreement within 0.1°C or less between our distribution and the global average from the model (**Fig S16**). These findings provide confidence that our dataset provides a reasonable approximation of global average temperature. Our results are also consistent with the work of Jones et al. (*85*) who demonstrated that the effective number of independent samples is reduced with timescale, where the global temperature field exhibits approximately 20 degrees of freedom on annual time scales, 10 on decadal, 5 on centennial, and even less on millennial timescales, suggesting that 73 points should capture much of the global temperature variability in our low frequency reconstruction.

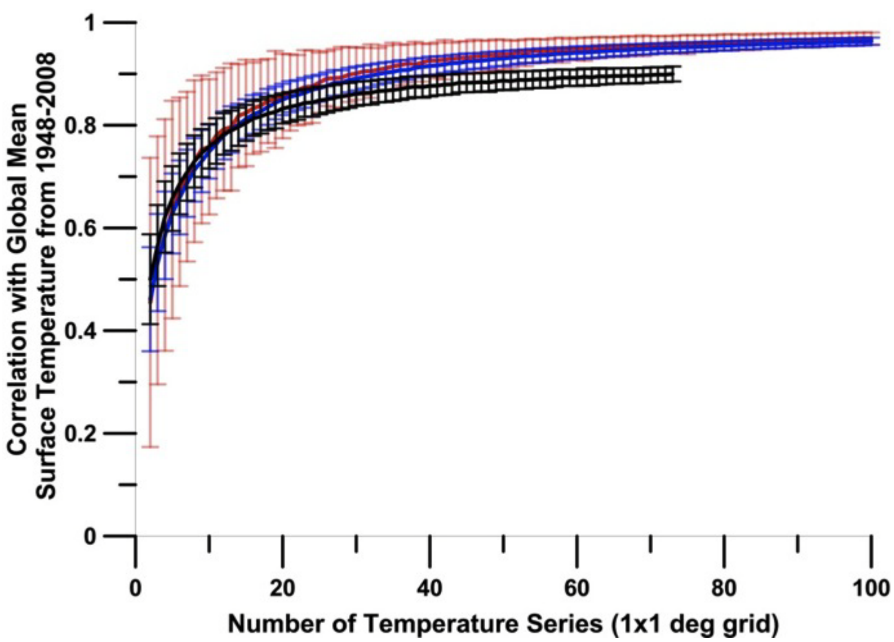

Fig. S13: Correlations with global mean surface temperature. Plotted is the mean (line) and 1σ uncertainty (bars) of the 1000 simulations. The red line represents the experiment where the grid points did not change through time for each of the 1000 simulations, the blue is when they change for each time step, and the black is the experiment where we used only grid boxes corresponding to the location of our global temperature data.

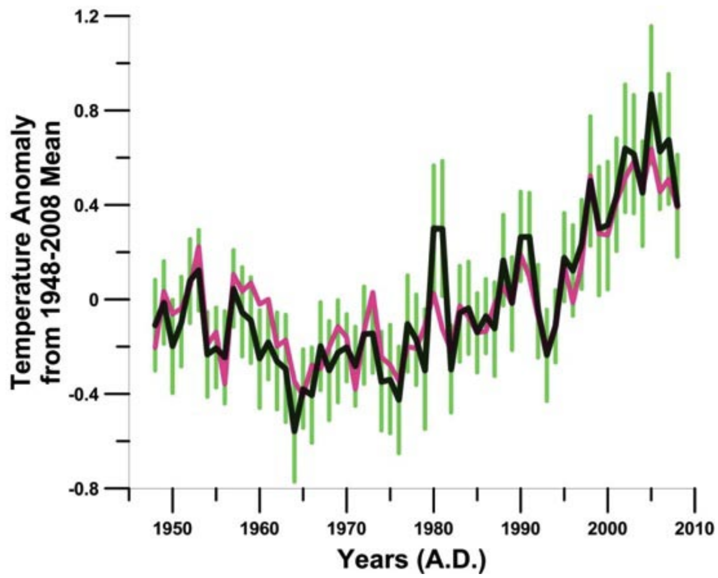

Fig. S14: Time series of global average temperature anomalies. The black line is the global average temperature anomaly from the NCEP NCAR reanalysis for 1948 to 2008. The pink line is the average temperature anomaly from the 73 grid points corresponding to the locations of our data sites. The green line, which is indistinguishable from the black, represents the average temperature anomaly at 73 randomly selected sites across the globe and the 2σ uncertainty of 1000 realizations (green bars).

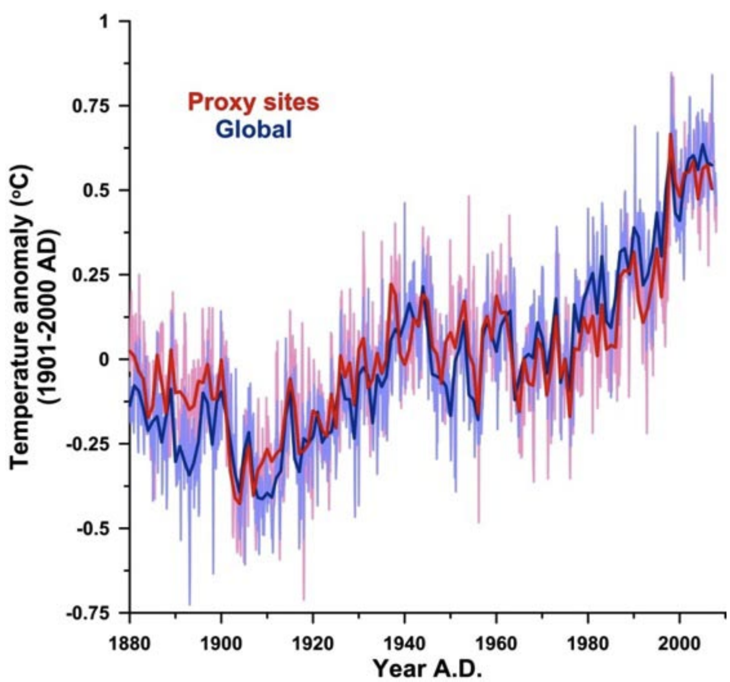

Fig. S15: Global mean temperature for the last 130 years (blue) and the mean temperature at the 73 proxy sites (red) from the NCDC blended land and ocean dataset (*84*). Light colored-lines show monthly values, while dark lines show annual means.

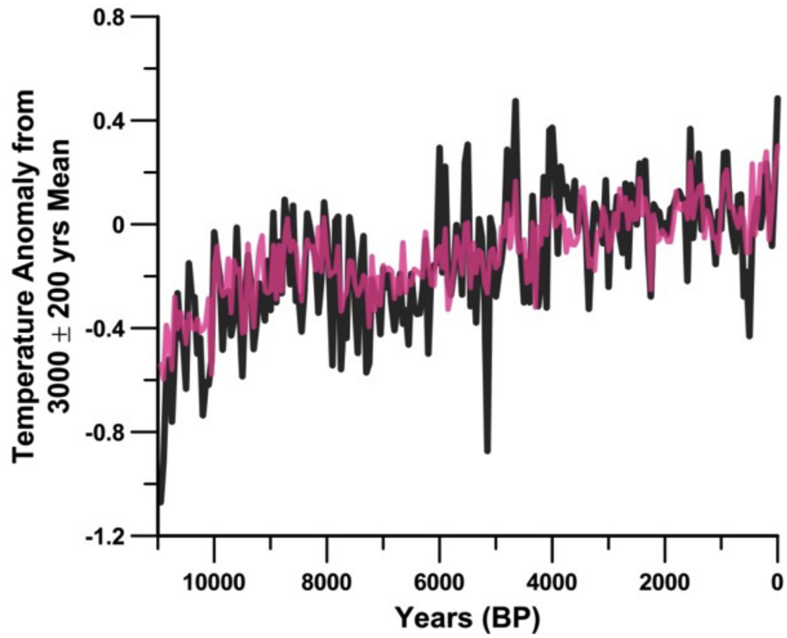

Fig. S16: Simulated global mean temperature for the last 11000 years (black) and the mean temperature at the 73 proxy sites (red) from the ECBilt-CLIO transient simulations (*81*).

9. Signal retention

Numerous factors work to smooth away variability in the temperature stack. These include temporal resolution, age model uncertainty, and proxy temperature uncertainty. We conducted a synthetic data experiment to provide a simple, first-order quantification of the reduction in signal amplitude due to these factors. We modeled each of the 73 proxy records as an identical annually-resolved white noise time series spanning the Holocene (i.e., the true signal), and then subsampled each synthetic record at 120-year resolution (the median of the proxy records) and perturbed it according to the temperature and age model uncertainties of the proxy record it represents in 100 Monte Carlo simulations. Power spectra of the resulting synthetic proxy stacks are red, as expected, indicating that signal amplitude reduction increases with frequency. Dividing the input white noise power spectrum by the output synthetic proxy stack spectrum yields a gain function that shows the fraction of variance preserved by frequency (**Fig. S17a**). The gain function is near 1 above ~2000-year periods, suggesting that multi-millennial variability in the Holocene stack may be almost fully recorded. Below ~300-year periods, in contrast, the gain is near-zero, implying proxy record uncertainties completely

remove centennial variability in the stack. Between these two periods, the gain function exhibits a steady ramp and crosses 0.5 at a period of ~1000 years.

Cross-spectral analysis of the input white noise and output synthetic stack shows that the time series are coherent and in phase at all frequencies (**Fig. S17b,c**), indicating that our Monte Carlo error-perturbation procedure does not artificially shift the amplitude or phase of input series.

We performed several sensitivity tests with this synthetic white noise experiment, exploring the effect of changing the magnitude of proxy age model uncertainties, temperature uncertainties, and temporal resolutions (**Fig. S18**). Results suggest that gain is negligibly influenced by temperature uncertainties, presumably because these errors largely cancel out in the large-scale stack. Gain is generally increased by shifting the resolution of the synthetic records from 120 to 20 years, though the amount varies with frequency. The largest increases in gain occur through reductions in age model uncertainty – shifting the 0.5 gain value to 1200-year periods by doubling age model errors and 800-year periods by halving age model errors – as would occur through decreasing radiocarbon measurement errors or increasing the density of radiocarbon dates.

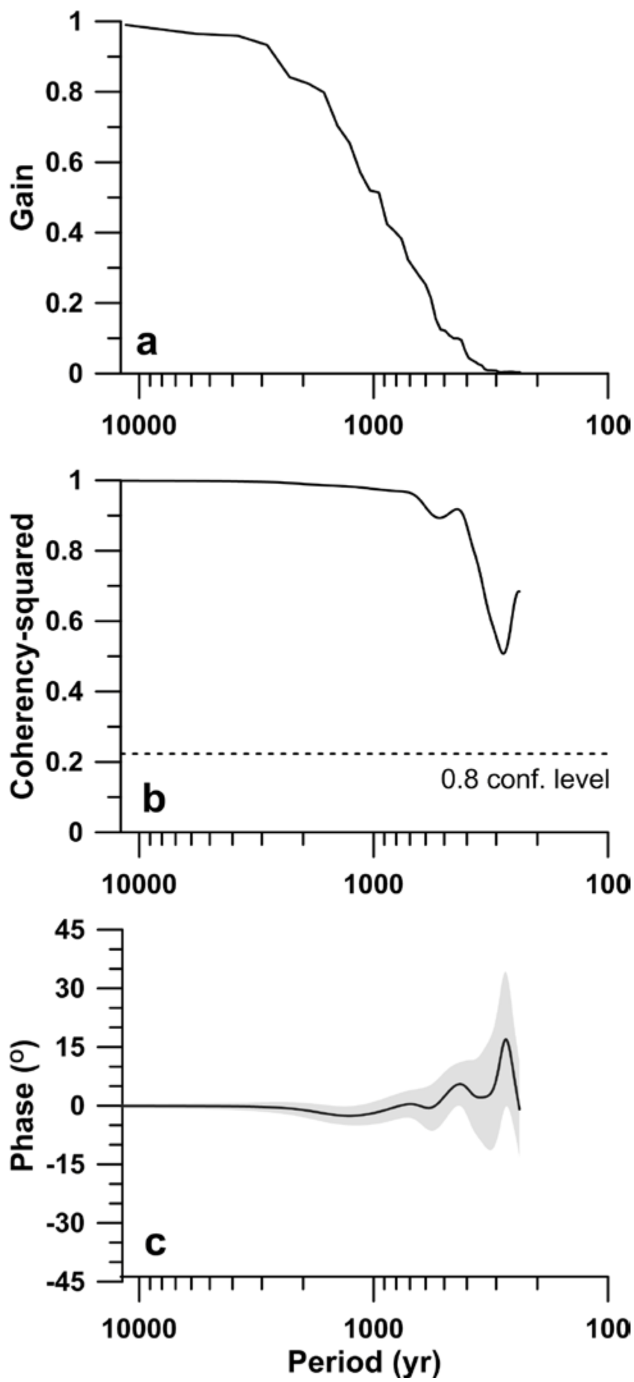

Fig. S17: Cross spectrum between an input white noise signal and an output synthetic stack perturbed according to the temperature and age models uncertainties of the proxy records and using a 120-year sampling resolution. **(a)** Gain, computed as the ratio of the variances of the synthetic stack and input white noise by frequency band. **(b)** Coherency squared. **(c)** Phase. Errors give 80% confidence intervals.

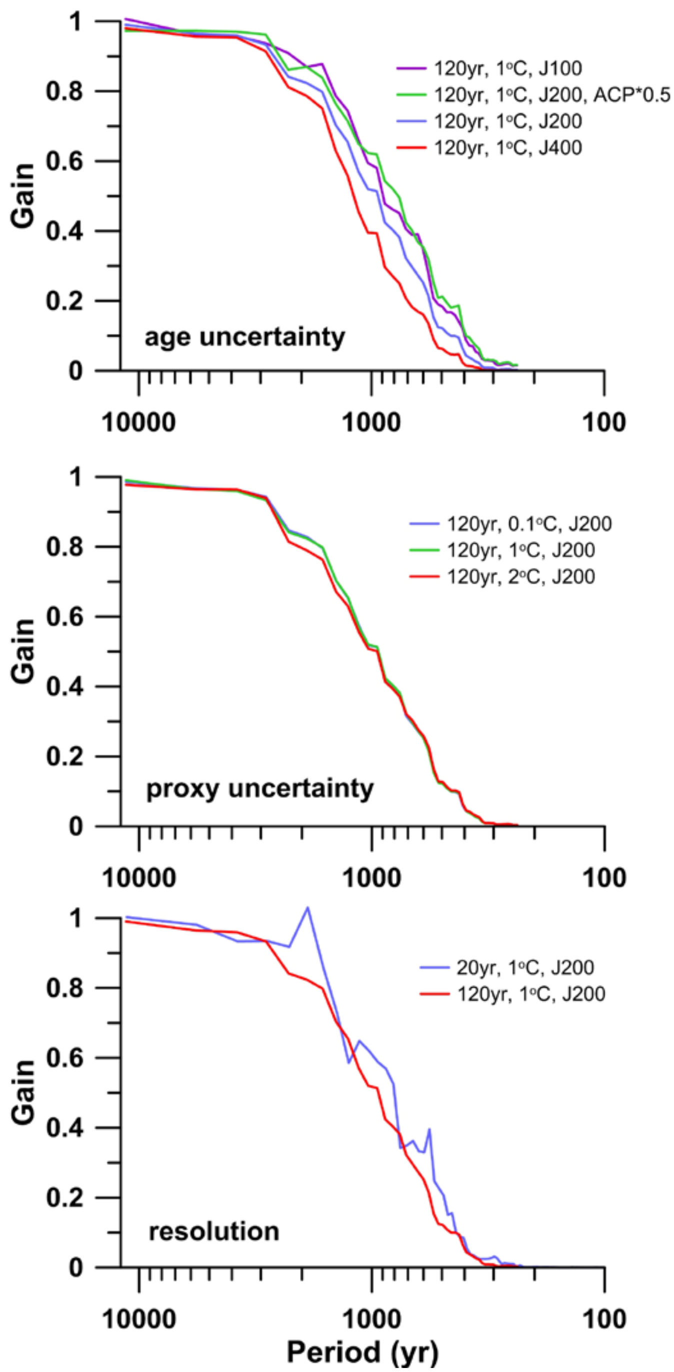

Fig. S18: Gain functions – computed as the ratio of variances in the output synthetic stack to input white noise by frequency band – assuming various levels of synthetic proxy data quality. The legend for each panel lists the following synthetic data parameters for each gain function: temporal resolution (yr), temperature uncertainty (°C), age model jitter value (J), and whether the error on age control points was halved (ACP*0.5). **(top)** Gain functions for varying chronologic uncertainty, **(middle)** temperature uncertainty, **(bottom)** and sampling resolution.

10. Mg/Ca Dissolution Bias

An increase in carbonate dissolution following the deglacial peak in carbonate preservation (*86*) could lead to the preferential removal of Mg-rich calcite, helping to explain the apparent long-term Holocene cooling in Mg/Ca records. We find no correlation between Mg/Ca-based temperature trends and core depth (**Fig. S19**), however, as might be expected if dissolution were an important factor.

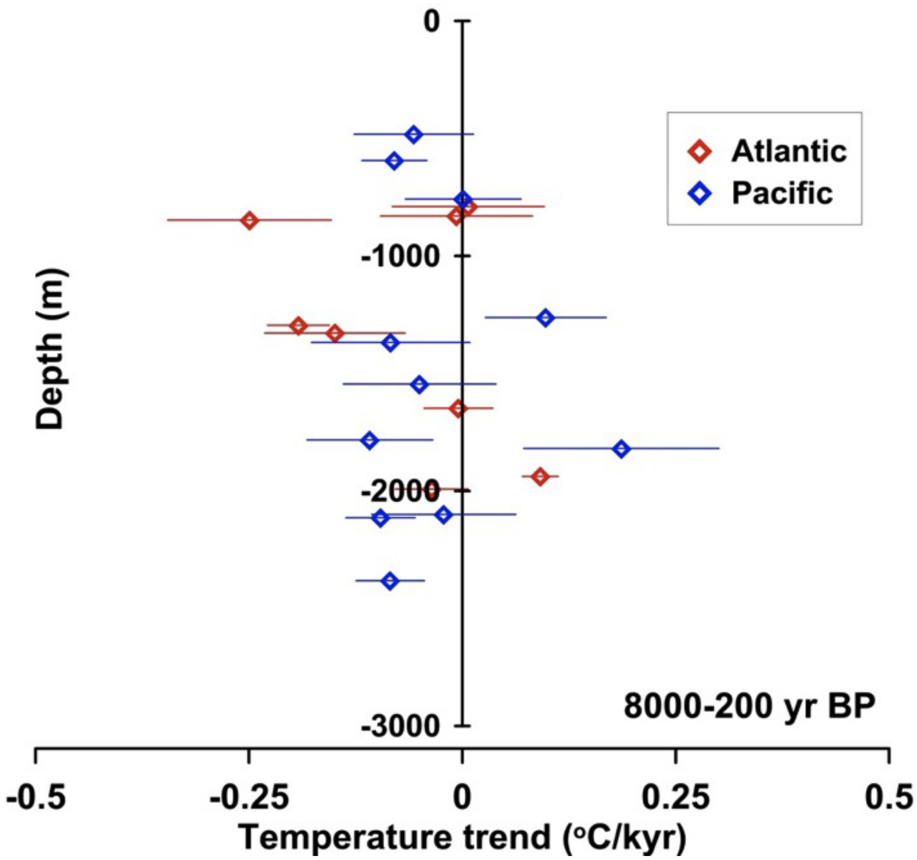

Fig. S19: Mg/Ca-based temperature trends from 8000-200 yr BP plotted against the ocean sediment core depths.

11. Adding High-Frequency Variability

The Holocene stack inherently under represents high-frequency variability due to, for example, the decadal to centennial-scale resolution of the proxy records, age-model uncertainty, bioturbation, etc. (see section 9). This missing variability is evident when comparing power spectra for the Holocene stack and the Mann et al. reconstruction (*2*) (**Fig. S20**). Both exhibit similar variance at multi-centennial time scales, but Mann et al. has considerably more power at higher frequencies.

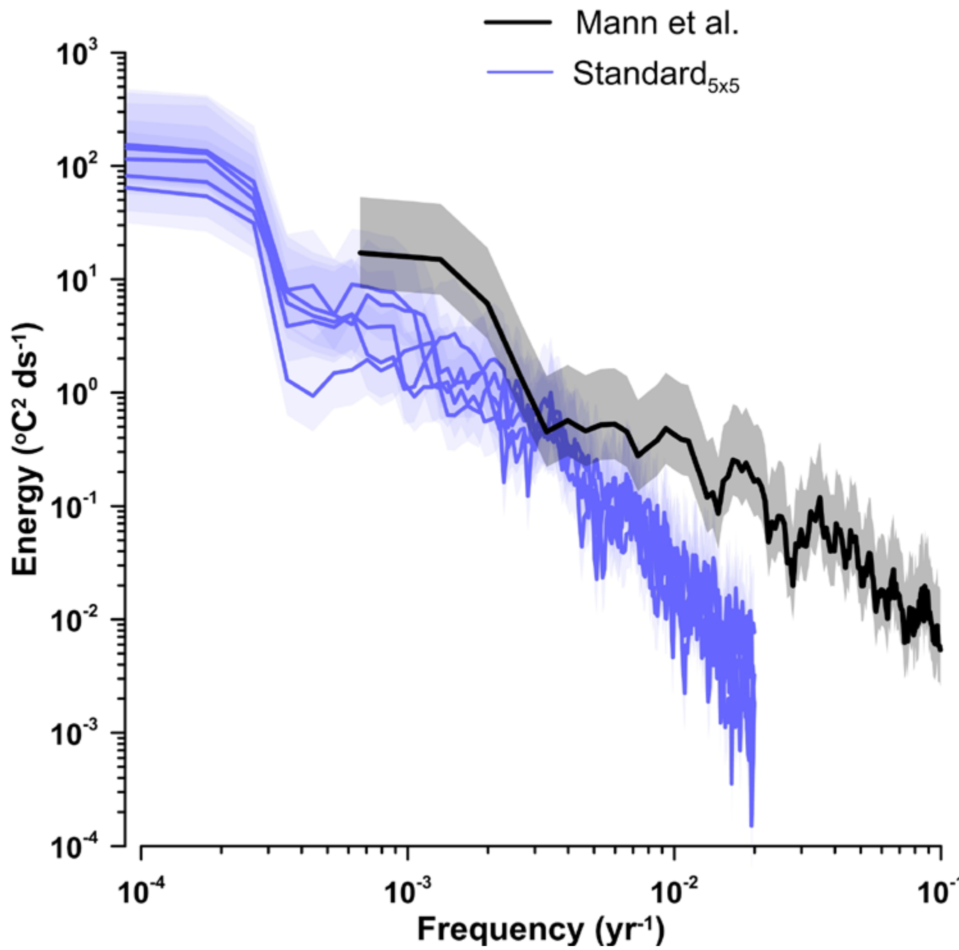

Fig. S20: Power spectra for 5 realizations of the Holocene temperature stack (blue) and the Mann et al. reconstruction (*2*) (black) calculated using the Thomson multi-taper method (code from http://www.people.fas.harvard.edu/~phuybers/Mfiles/index.html). Shading gives 95% confidence intervals. Bandwidth (ds) is one over the length of the record in years.

To examine the sensitivity of our main conclusions to this missing variability, we use the Mann et al. reconstruction (*2*) to add the amount of high-frequency variability exhibited in global temperature over the past 1500 years to the Holocene stack (1) as white noise and (2) as red noise. Our aim is to determine how much this missing variability may widen the Holocene temperature distribution.

We first high-pass filter the Mann et al. reconstruction, excluding the post-1900 AD interval to avoid the large anthropogenically forced signal over this time (**Fig. S21**). A histogram of the resulting time series reflects the distribution of high-frequency variability around the long-term, millennial-scale mean (**Fig S21**). We then low-pass filter the Holocene stack with a 1000-year cutoff, and add noise to each data point in the resulting time series randomly drawn from the high-pass filtered Mann et al. histogram. Since it is unclear whether high-frequency variability over the past 1500 years adequately represents high-frequency variability earlier in the Holocene, we also repeat this procedure after widening the high-pass filtered Mann et al. histogram by a factor of 2. We also redo the analysis using a 300-year, rather than 1000-year, filter, and obtain nearly identical results (**Fig. S22**).

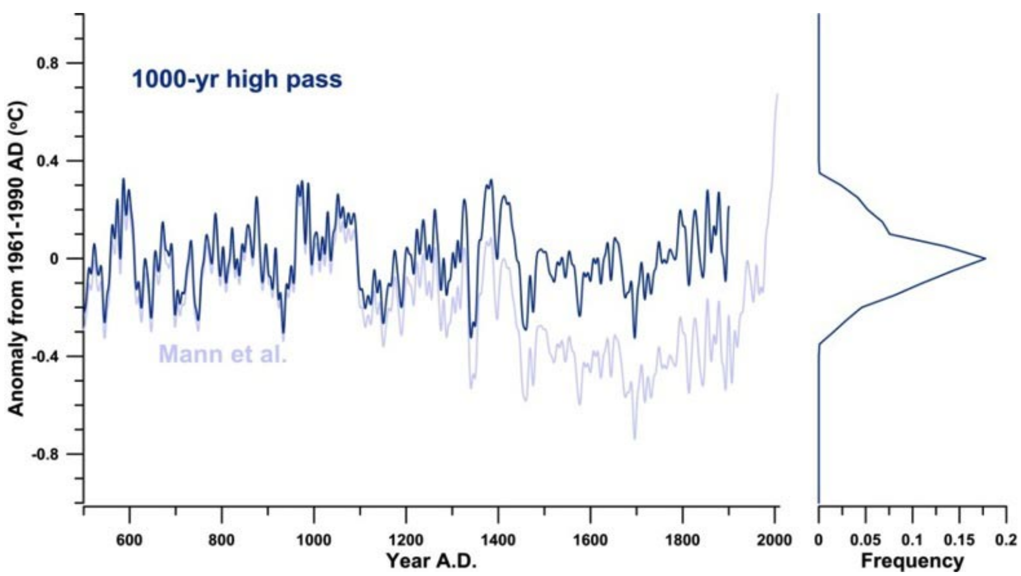

Fig. S21: (left) The raw (light blue) and 1000-year high pass filtered (dark blue) Mann et al. reconstruction. (right) Frequency plot of the high pass filtered temperature anomalies.

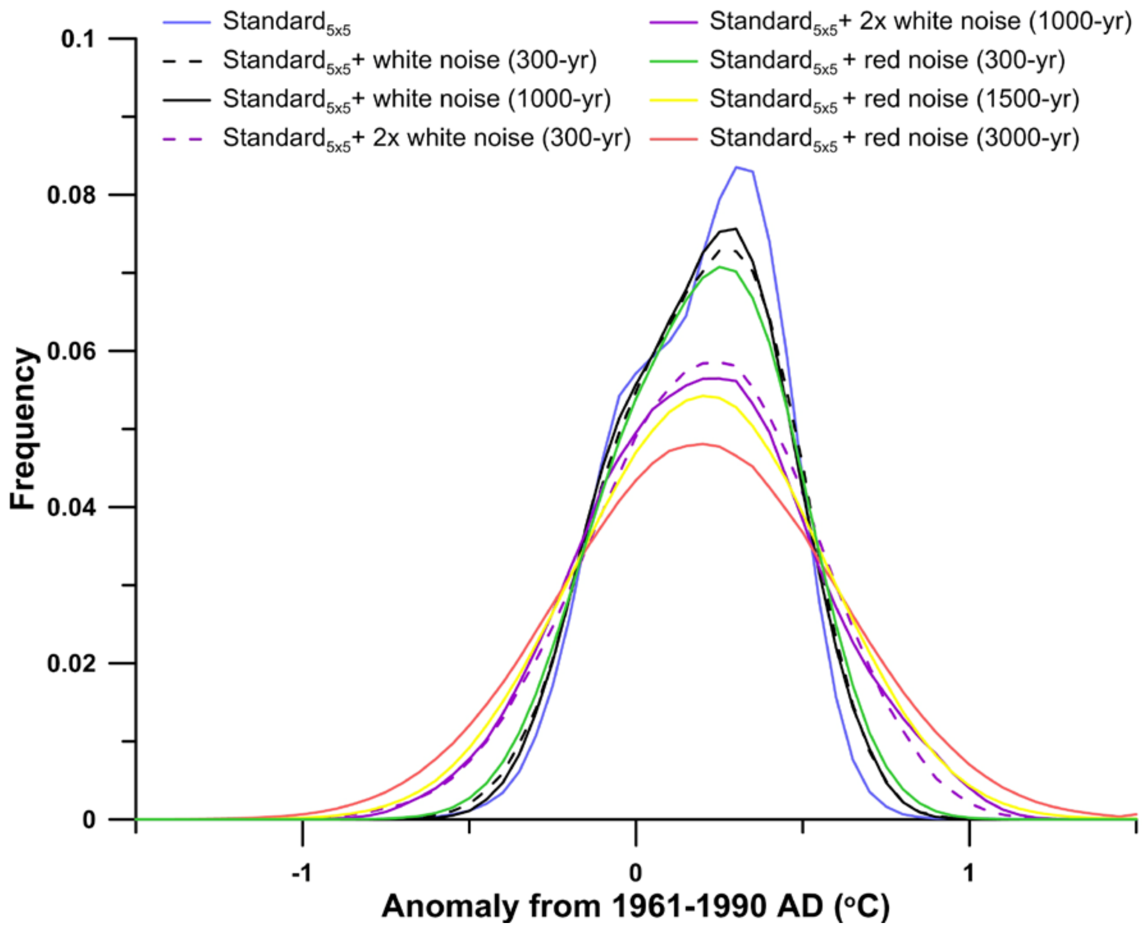

Fig. S22: Holocene temperature distributions based on 1000 realizations of the Standard$_{5x5}$ stack (blue), and after adding 1x (black) and 2x (purple) the high-frequency variability observed in the Mann et al. reconstruction as white noise as well as adding red noise with the same power distribution as Mann et al. The dashed (solid) lines are based on using a 300-year (1000-year) filter in the white noise addition procedure.

We also add red noise to the Holocene stack using an AR-1 model that yields the same general spectral distribution of power as the Mann et al. reconstruction (**Fig. S23**). As above, we try several different cutoff periodicities when filtering the Holocene stacks and AR-1 time series prior to adding the noise.

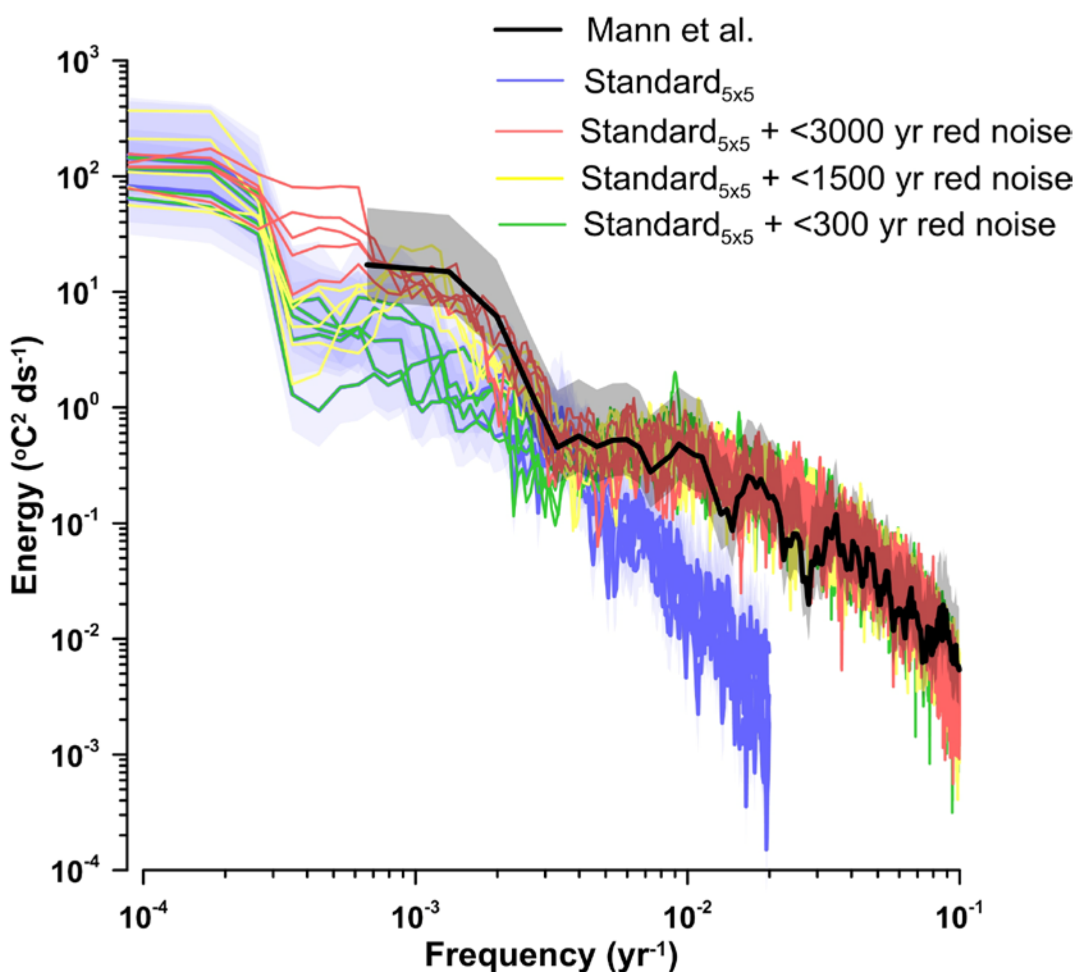

Fig. S23: Power spectra for five realization of the Standard$_{5x5}$ stack (blue) and the Mann et al. reconstruction (black), as in Figure S21. Also shown are spectra for these five realizations after adding red noise for periods less than 3000 (red), 1500 (yellow), and 300 (green) years.

These two approaches suggest that while assumptions about the amount and distribution of high-frequency variability can change the width of the Holocene temperature distribution, the effects are relatively modest and do not affect our conclusion that current global temperature is near the warmer end of the Holocene spectrum and 2100 AD temperature will be beyond the warmest of the Holocene (**Fig. S24)**. For instance, the standard deviation of the Standard$_{5x5}$ Holocene distribution increases from 0.24°C to 0.37°C after adding red noise for periods less than 1500 years.

To provide an additional check on our inference that the Holocene temperature distribution is only modestly decreased due to limitations of our proxy database, we also

generated a pseudoproxy database using Holocene output from the ECBilt-CLIO intermediate complexity model. We sampled the model at the same locations as the proxy records and degraded the output using the resolution, chronologic uncertainties, and temperature uncertainties of the real proxy records through 200 Monte Carlo simulations (**Fig. S24**). The temperature anomaly distribution of the resulting pseudoproxy temperature stacks is nearly identical to that of the actual annual global temperature time series in the model. This similarity suggests that the limited spatial and temporal sampling of our Holocene dataset does not lead it to underestimate the range of Holocene temperature variability; presumably, the uncertainty perturbations assigned during the Monte Carlo procedure compensate for the reduced data coverage and increase its variability.

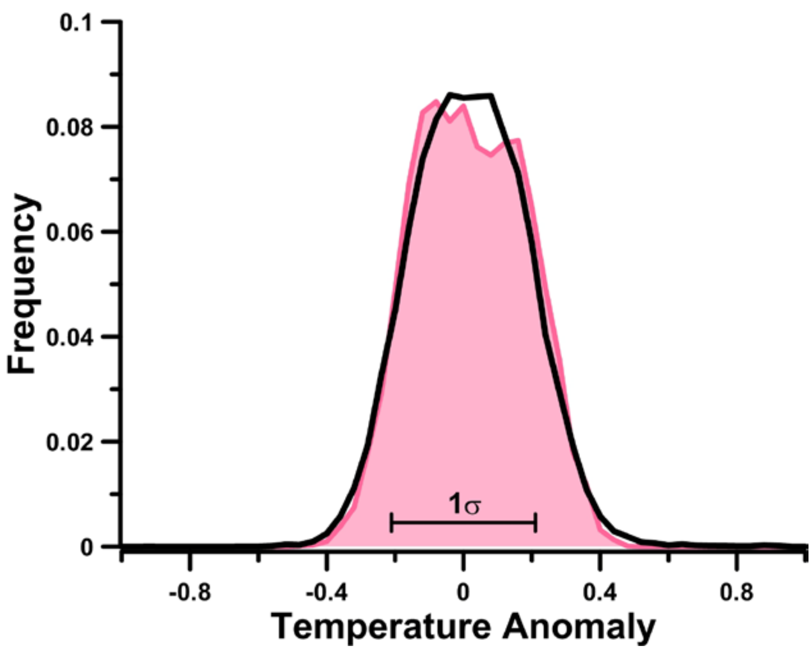

Fig. S24: Pseudoproxy temperature anomaly (0 – 10,000 yr BP) distributions from the ECBilt-CLIO intermediate complexity model results based on 200 realizations of the Standard_{5x5} stack (black). The red, filled curve represents the temperature anomalies of the entire (i.e. global) model domain.

12. Data-Model Comparison

We compared our global and regional temperature stacks with a transient modeling experiment using the ECBilt-CLIO intermediate complexity model (*81*). Comparing our Standard 5x5° global stack to the simulated annual surface temperatures at our proxy locations, there is agreement within 0.1°C between the data and model in the early Holocene, but after 5,000 yrs BP the data and model diverge; the data suggest a cooling of 0.8°C toward the late Holocene and the model simulates a slight warming of ~0.2°C (**Fig. S25a**). Comparing the temperature data and model simulations by region demonstrates that the largest data-model disagreement is in the mid-high latitude Northern Hemisphere sites while the data and model in the equatorial and mid-high latitude Southern Hemisphere sites are in agreement within the Monte Carlo based uncertainty after 9,000 yrs BP (**Fig. S25b,c,d**). When the North Atlantic proxy sites that show the largest temperature changes are removed, the data and model are within the Monte Carlo based uncertainty, both in the global stack and the mid-high latitude northern hemisphere stack (**Fig. S26a,b**).

The data-model disagreement may suggest that the model could be missing a key climate component that is intrinsic to the North Atlantic basin. In particular, the AMOC may have slowed during the Holocene, resulting in an amplified cooling in the North Atlantic basin and a warming in the Southern Hemisphere that could have dampened any cooling effect expected from orbital tilt (*87-89*). Further transient modeling that simulates a reduction in the AMOC during the Holocene should help clarify whether such changes could be the primary source of the data-model discrepancy highlighted in this experiment.

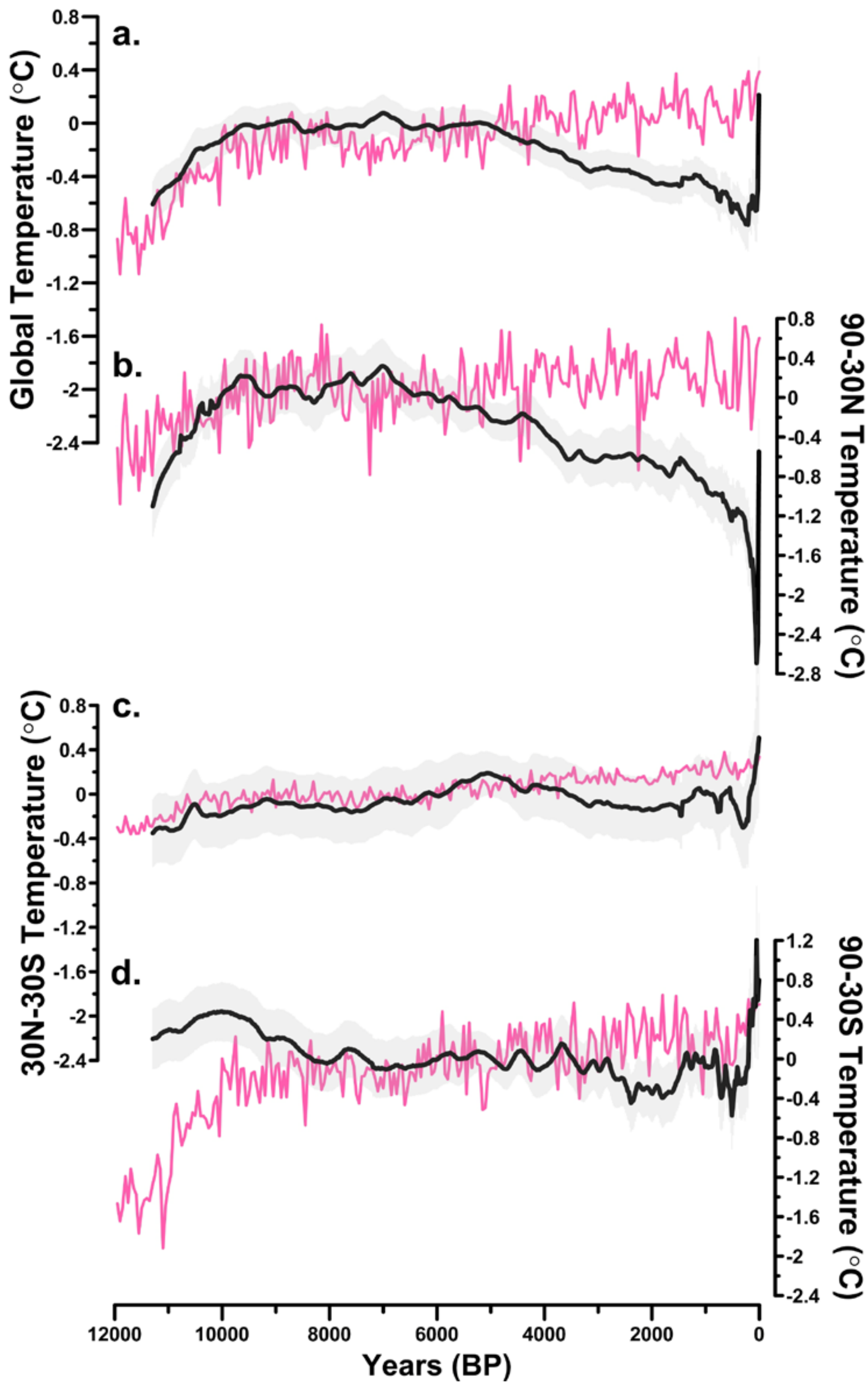

Fig. S25: Simulated global and regional mean temperatures for the last 12000 years (red) from the ECBilt-CLIO transient simulations (*81*) and the Standard 5x5° weighted temperature stack from the proxy dataset from this study (black). The temperature is an anomaly from 6,000 yrs BP (± 200 yrs).

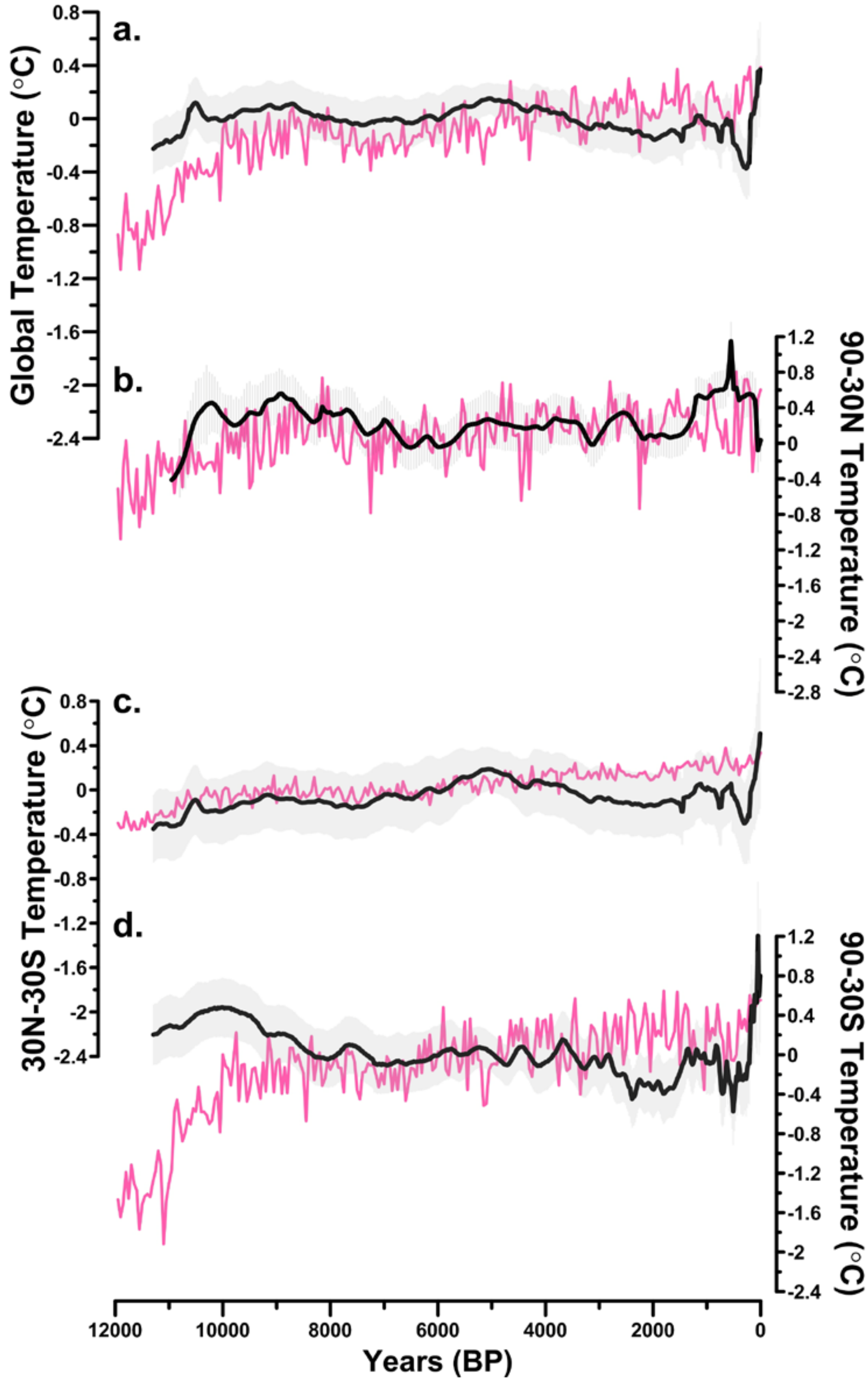

Fig. S26: Simulated global and regional mean temperatures for the last 12000 years (red) from the ECBilt-CLIO transient simulations (*81*) and the Standard 5x5° weighted temperature stack with the North Atlantic sites removed (black). The temperature is an anomaly from 6,000 yrs BP (± 200 yrs).

References

1. P. J. Reimer, Baillie, M. G. L., Bard, E., Bayliss, A., Beck, J. W., Blackwell, P. G., Bronk Ramsey, C., Buck, C. E., Burr, G. S., Edwards, R. L., Friedrich, M., Grootes, P. M., Guilderson, T. P., Hajdas, I., Heaton, T. J., Hogg, A. G., Hughen, K. A., Kaiser, K. F., Kromer, B., McCormac, F. G., Manning, S. W., Reimer, R. W., Richards, D. A., Southon, J. R., Talamo, S., Turney, C. S. M., van der Plicht, J., and Weyhenmeyer, C.E., INTCAL 09 and MARINE09 radiocarbon age calibration curves, 0-50,000 years Cal BP. *Radiocarbon* **51**, 1111 (2009).
2. M. E. Mann *et al.*, Proxy-based reconstructions of hemispheric and global surface temperature variations over the past two millennia. *Proceedings of the National Academy of Sciences* **105**, 13252 (2008).
3. P. J. Müller, G. Kirst, G. Ruthland, I. von Storch, A. Rosell-Melé, Calibration of the alkenone paleotemperature index UK'37 based on core-tops from the eastern South Atlantic and the global ocean (60N-60S). *Geochimica et Cosmochimica Acta* **62**, 1757 (1998).
4. H. W. Arz, J. Pätzold, P. J. Müller, Influence of Northern Hemisphere climate and global sea level rise on the restricted Red Sea marine environment during termination I. *Paleoceanography* **18**, doi:10.1029/2002PA000864 (2003).
5. J. A. Barron, L. Heusser, T. Herbert, M. Lyle, High resolution climatic evolution of coastal northern California during the past 16,000 years. *Paleoceanography* **18**, 20 (2003).
6. T. T. Barrows, S. J. Lehman, L. K. Fifield, P. De Deckker, Absence of Cooling in New Zealand and the Adjacent Ocean During the Younger Dryas Chronozone. *Science* **318**, 86 (2007).
7. J. A. P. Bendle, A. Rosell-Mele, High-resolution alkenone sea surface temperature variability on the North Icelandic Shelf: implications for Nordic Seas palaeoclimatic development during the Holocene. *The Holocene* **17**, 9 (2007).
8. P. Anand, H. Elderfield, M. H. Conte, Calibration of Mg/Ca thermometry in planktonic foraminifera from a sediment trap time series. *Paleoceanography* **18**, doi:10.1029/2002PA000846 (2003).
9. H. M. Benway, A. C. Mix, B. A. Haley, G. P. Klinkhammer, Eastern Pacific Warm Pool paleosalinity and climate variability: 0 – 30 kyr. *Paleoceanography* **21**, PA3008 (2006).
10. I. Cacho *et al.*, Variability of the western Mediterranean Sea surface temperature during the last 25,000 years and its connection with the Northern Hemisphere climatic changes. *Paleoceanography* **16**, 40 (2001).
11. E. Calvo, J. Grimalt, E. Jansen, High resolution UK37 sea surface temperature reconstruction in the Norwegian Sea during the Holocene. *Quaternary Science Review* **21**, 1385 (2002).
12. R. E. Came, D. W. Oppo, J. F. McManus, Amplitude and timing of temperature and salinity variability in the subpolar North Atlantic over the past 10 k.y. *Geology* **35**, 315 (2007).
13. J.-H. Kim, S. Schouten, E. C. Hopmans, B. Donner, J. S. Sinninghe Damsté, Global sediment core-top calibration of the TEX86 paleothermometer in the ocean. *Geochimica et Cosmochimica Acta* **72**, 1154 (2008).
14. I. S. Castañeda *et al.*, Millennial-scale sea surface temperature changes in the eastern Mediterranean (Nile River Delta region) over the last 27,000 years. *Paleoceanography* **25**, PA1208 (2010).
15. B. F. Clegg *et al.*, Six millennia of summer temperature variation based on midge analysis of lake sediments from Alaska. *Quaternary Science Review*, doi:10.1016/j.quascirev.2010.08.001 (2010).
16. P. deMenocal, J. Ortiz, T. Guilderson, M. Sarnthein, Coherent High- and Low-Latitude climate variability during the Holocene warm period. *Science* **288**, 2198 (2000).

17. J. K. Dolven, G. Cortese, K. R. Bjøklund, A high-resolution radiolarian-derived paleotemperature record for the Late Pleistocene-Holocene in the Norwegian Sea. *Paleoceanography* **17**, doi:10.1029/2002PA000780 (2002).
18. K. C. Emeis, U. Struck, T. Blanz, A. Kohly, M. Woß, Salinity changes in the central Baltic Sea (NW Europe) over the last 10 000 years. *The Holocene* **13**, 411 (2003).
19. T. A. Mashiotta, D. W. Lea, H. J. Spero, Glacial-interglacial changes in Subantarctic sea surface temperature and d18O-water using foraminiferal Mg. *Earth and Planetary Science Letters* **170**, 417 (1999).
20. E. C. Farmer, P. B. deMendocal, T. M. Marchitto, Holocene and deglacial ocean temperature variability in the Benguela upwelling region: Implications for low-latitude atmospheric circulation. *Paleoceanography* **20**, doi:10.1029/2004PA001049 (2005).
21. S. Giunta, K. C. Emeis, A. Negri, Sea-surface temperature reconstruction of the last 16,000 years in the Eastern Mediterranean Sea. *Rivista Italiana di Paleontologia e Stratigrafia* **107**, 463 (2001).
22. C. Huguet, J.-H. Kim, J. S. S. Damsté, S. Schouten, Reconstruction of sea surface temperature variations in the Arabian Sea over the last 23 kyr using organic proxies (TEX86 and UK37). *Paleoceanography* **21**, doi:10.1029/2005PA001215 (2006).
23. S. Schouten, E. C. Hopmans, E. Schefuß, J. S. Sinninghe Damsté, Distributional variations in marine crenarchaeotal membrane lipids: A new tool for reconstructing ancient sea water temperatures? *Earth and Planetary Science Letters* **204**, 265 (2002).
24. G. Isono *et al.*, The 1500-year climate oscillation in the midlatitude North Pacific during the Holocene. *Geology* **37**, 591 (2010).
25. A. Jaeschke, C. Rühlemann, H. Arz, G. Heil, G. Lohmann, Coupling of millennial-scale changes in sea surface temperature and precipitation off northeastern Brazil with high-latitude climate shifts during the last glacial period. *Paleoceanography* **22**, doi:10.1029/2006PA001391 (2007).
26. J. Jouzel *et al.*, Orbital and Millennial Antarctic Climate Variability over the Past 800,000 Years. *Science* **317**, 793 (2007).
27. J. Kaiser, E. Schefuß, F. Lamy, M. Mohtadi, D. Hebbeln, Glacial to Holocene changes in sea surface temperature and coastal vegetation in north central Chile: high versus low latitude forcing. *Quaternary Science Review* **27**, 2064 (2008).
28. K. Kawamura *et al.*, Northern Hemisphere forcing of climatic cycles in Antarctica over the past 360,000 years. *Nature* **448**, 912 (2007).
29. M. Kienast, S. Steinke, K. Stattegger, S. E. Calvert, Synchronous Tropical South China Sea SST Change and Greenland Warming During Deglaciation. *Science* **291**, 2132 (2001).
30. J.-H. Kim, R. R. Schneider, P. J. Muller, G. Wefer, Interhemispheric comparison of deglacial sea-surface temperature patterns in Atlantic eastern boundary currents. *Earth and Planetary Science Letters* **194**, 383 (2002).
31. J.-H. Kim *et al.*, North Pacific and North Atlantic sea-surface temperature variability during the Holocene. *Quaternary Science Review* **23**, 2141 (2004).
32. Y. Kubota *et al.*, Variations of East Asian summer monsoon since the last deglaciation based on Mg/Ca and oxygen isotope of planktic foraminifera in the northern East China Sea. *Paleoceanography* **25**, doi:10.1029/2009PA001891 (2010).
33. J. Kurek, L. Cwynar, J. C. Vermaire, A late Quaternary paleotemperature record from Hanging Lake, northern Yukon Territory, eastern Beringia. *Quaternary Research* **72**, 246 (2009).
34. F. Lamy, C. Rühlemann, D. Hebbein, G. Wefer, High- and low-latitude climate control on the position of the southern Peru-Chile Current during the Holocene. *Paleoceanography* **17**, 10.1029/2001PA000727 (2002).

35. I. Larocque, R. I. Hall, Holocene temperature estimates and chironomid community composition in the Abisko Valley, northern Sweden. *Quaternary Science Review* **23**, 2453 (2004).
36. D. W. Lea, D. K. Pak, L. C. Peterson, K. A. Hughen, Sychroneity of Tropical and High-Latitude Atlantic Temperatures over the Last Glacial Termination. *Science* **301**, 1361 (2003).
37. G. Leduc *et al.*, Moisture transport across Central America as a positive feedback on abrupt climatic changes. *Nature* **445**, 908 (2007).
38. P. S. Dekens, D. W. Lea, D. K. Pak, H. J. Spero, Core top calibration of Mg/Ca in tropical foraminifera: Refining paleotemperature estimation. *Geochemistry, Geophysics, and Geosystems* **3**, doi:10.1029/2001GC000200 (2002).
39. C. Levi *et al.*, Low-latitude hydrological cycle and rapid climate changes during the last deglaciation. *Geochemistry, Geophysics, and Geosystems* **8**, Q05N12 (2007).
40. B. K. Linsley, Y. Rosenthal, D. W. Oppo, Holocene evolution of the Indonesian throughflow and the western Pacific warm pool. *Nature Geoscience* **3**, 578 (2010).
41. O. Marchal *et al.*, Apparentlong-termcoolingoftheseasurfaceinthenortheast Atlantic and Mediterranean during the Holocene. *Quaternary Science Review* **21**, 455 (2002).
42. M. S. McGlone, C. S. M. Turney, J. M. Wilmshurst, J. Renwick, K. Pahnke, Divergent trends in land and ocean temperature in the Southern Ocean over the past 18,000 years. *Nature Geoscience* **3**, 622 (2010).
43. M. Mohtadi, S. Steinke, A. Lückge, J. Groeneveld, E. C. Hathorne, Glacial to Holocene surface hydrography of the tropical eastern Indian Ocean. *Earth and Planetary Science Letters* **292**, 89 (2010).
44. S. H. H. Nielsen, N. Koç, X. Crosta, Holocene climate in the Atlantic sector of the Southern Ocean: Controlled by insolation or oceanic circulation? *Geology* **32**, 317 (2010).
45. K. Pahnke, J. P. Sachs, Sea surface temperatures of southern midlatitudes 0 – 160 kyr B. P. *Paleoceanography* **21**, PA2003 (2006).
46. C. Pelejero, J. Grimalt, S. Heilig, M. Kienast, L. Wang, High resolution UK37 temperature reconstructions in the South China Sea over the past 220 kyr. *Paleoceanography* **14**, 224 (1999).
47. J. R. Petit, Climate and Atmospheric history of the past 420,000 years from the Vostok ice core, Antarctic. *Nature* **399**, 429 (1999).
48. T. Rodrigues, J. O. Grimalt, F. G. Abrantes, J. A. Flores, S. M. Lebreiro, Holocene interdependences of changes in sea surface temperature, productivity, and fluvial inputs in the Iberian continental shelf (Tagus mud patch). *Geochemistry, Geophysics, and Geosystems* **10**, Q07U06 (2009).
49. C. Rühlemann, S. Mulitza, P. J. Muller, G. Wefer, R. Zahn, Warming of the tropical Atlantic Ocean and slowdown of thermohaline circulation during the last deglaciation. *Nature* **402**, 511 (1999).
50. J. P. Sachs, Cooling of Northwest Atlantic slope waters during the Holocene. *Geophysical Research Letters* **34**, L03609 (2007).
51. M. Sarnthein *et al.*, Overview of Glacial Atlantic Ocean Mapping (GLAMAP 2000). *Paleoceanography* **18**, 10.1029/2002PA000769 (2003).
52. E. Schefuß, S. Schouten, R. R. Schneider, Climatic controls on central African hydrology during the past 20,000 years. *Nature* **437**, 1003 (2005).
53. H. Seppä, D. Hammarlund, K. Antonsson, Low-frequency and high-frequency changes in temperature and effective humidity during the Holocene in south-central Sweden: implications for atmospheric and oceanic forcings of climate. *Climate Dynamics* **25**, 285 (2005).
54. H. Seppä, H. J. B. Birks, July mean temperature and annual precipitation trends during the Holocene in the Fennoscandian tree-line area: pollen-based climate reconstructions. *The Holocene* **11**, 527 (2001).

55. H. Seppä, J. Weckström, Holocene vegetational and limnological changes in the Fennoscandian tree-line area as documented by pollen and diatom records from Lake Tsuolbmajavri, Finland. *Ecoscience* **6**, 621 (1999).
56. S. Steinke *et al.*, Proxy dependence of the temporal pattern of deglacial warming in the tropical South China Sea: toward resolving seasonality. *Quaternary Science Review* **27**, 688 (2008).
57. B. Stenni *et al.*, The deuterium excess records of EPICA Dome C and Dronning Maud Land ice cores (East Antarctica). *Quaternary Science Review* **29**, 146 (2010).
58. L. Stott, A. Timmerman, R. Thunell, Southern hemisphere and deep-sea warming led deglacial atmospheric CO2 rise and tropical warming. *Science* **318**, 435 (2007).
59. Y. Sun, D. W. Oppo, R. Xiang, W. Liu, S. Gao, Last deglaciation in the Okinawa Trough: Subtropical northwest Pacific link to Northern Hemisphere and tropical climate. *Paleoceanography* **20**, PA4005 (2005).
60. D. J. R. Thornalley, H. Elderfield, I. N. McCave, Holocene oscillations in temperature and salinity of the surface subpolar North Atlantic. *Nature* **457**, (2009).
61. L. Powers, T. C. Johnson, J. P. Werne, I. S. Castaneda, Hopmans, E. C., Sinninghe Damste, J. S., and Schouten, S., Large termperature variability in the southern African tropics since the Last Glacial Maximum. *Geophysical Research Letters* **32**, doi:10.1029/2004GL022014 (2005).
62. J. E. Tierney *et al.*, Northern Hemisphere Controls on Tropical Southeast African Climate During the Past 60,000 Years. *Science* **322**, 252 (2008).
63. B. M. Vinther *et al.*, Holocene thinning of the Greenland ice sheet. *Nature* **461**, 385 (2009).
64. J. W. H. Weijer, E. Schefuß, S. Schouten, J. S. D. Damste, Coupled Thermal and Hydrological Evolution of Tropical Africa over the Last Deglaciation. *Science* **315**, 1701 (2007).
65. S. Weldeab, D. W. Lea, R. R. Schneider, N. Andersen, 155,000 Years of West African Monsoon and Ocean Thermal Evolution. *Science* **316**, 1303 (2007).
66. S. Weldeab, R. R. Schneider, M. Kölling, Deglacial sea surface temperature and salinity increase in the western tropical Atlantic in synchrony with high latitude climate instabilities. *Earth and Planetary Science Letters* **241**, 699 (2006).
67. S. Weldeab, R. R. Schneider, M. Kölling, G. Wefer, Holocene African droughts relate to eastern equatorial Atlantic cooling. *Geology* **33**, 981 (2005).
68. J. Xu, A. Holbourn, W. Kuhnt, Z. Jian, H. Kawamura, Changes in the thermocline structure of the Indonesian outflow during Terminations I and II. *Earth and Planetary Science Letters* **273**, 152 (2008).
69. M. Ziegler, D. Nürnberg, C. Karas, R. Tiedemann, L. J. Lourens, Persistent summer expansion of the Atlantic Warm Pool during glacial abrupt cold events. *Nature Geoscience* **1**, 601 (2008).
70. E. M. Barley *et al.*, A northwest North American training set: distribution of freshwater midges in relation to air temperature and lake depth. *Journal of Paleolimnology* **36**, 295 (2006).
71. W. I. Palmer SL, Heinrichs ML, Hebda R, Scudder G, Postglacial midge community change and Holocene palaeotemperature reconstructions near treeline, southern British Columbia (Canada). *Journal of Paleolimnology* **28**, 469 (2002).
72. W. I. Rosenberg SM, Mathewes RW, Hallett DJ, Midge-inferred Holocene climate history of two subalpine lakes in southern British Columbia. *Holocene* **14**, 258 (2004).
73. L. A. Walker IR, Cwynar LC, Lotter AF, An expanded surface-water palaeotemperature inference model for use with fossil midges from eastern Canada. *Journal of Paleolimnology* **18**, 165 (1997).
74. I. Larocque, How many chironomid head capsules are enough? A statistical approach to determine sample size for palaeoclimatic reconstructions. *Paleogeography, Palaeoclimatology, Palaeoecology* **172**, 133 (2001).

75. C. Bigler, R. I. Hall, Diatoms as indicators of climatic and limnological change in Swedish Lapland: a 100-lake calibration-set and its validation for paleoecological reconstructions. *Journal of Paleolimnology* **27**, 97 (2002).
76. P. Huybers, C. Wunch, A depth-derived Pleistocene age model: Uncertainty estimates, sedimentation variability, and nonlinear climate change. *Paleoceanography* **19**, PA1028 (2004).
77. J. D. Shakun *et al.*, Global warming preceded by increasing carbon dioxide concentrations during the last deglaciation. *Nature* **484**, 49 (2012).
78. T. Schneider, Analysis of incomplete climate data: Estimation of mean values and covariance matrices and imputation of missing values. *Journal of Climate* **14**, 853 (2001).
79. A. Mix, Running hot and cold in the eastern equatorial Pacific. *Quaternary Science Reviews* **25**, 1147 (2006).
80. G. Leduc, R. Schneider, J.-H. Kim, G. Lohmann, Holocene and Eemian sea surface temperature trends as revealed by alkenone and Mg/Ca paleothermometry. *Quaternary Science Review* **29**, 989 (2010).
81. O. Timm, A. Timmerman, Simulation of the last 21,000 years using accelerated transient boundary conditions. *Journal of Climate* **20**, 4377 (2007).
82. N. G. Pisias, A. C. Mix, Aliasing of the geologic record and the search for long-period Milankovitch cycles. *Paleoceanography* **3, No. 5**, 613 (1988).
83. E. Kalnay *et al.*, The NCEP/NCAR 40-year Reanalysis Project. *Bulletin of the American Meteorological Society* **77**, 437 (1996).
84. T. M. Smith, R. W. Reynolds, T. C. Peterson, J. Lawrimore, Improvements to NOAA's Historical Merged Land-Ocean Surface Temperature Analysis (1880-2006). *Journal of Climate* **21**, 2283 (2008).
85. P. D. Jones, T. J. Osborn, K. R. Briffa, Estimating sampling errors in large-scale temperature averages. *Journal of Climate* **10**, 2548 (1997).
86. W. H. Berger, Deep-sea carbonate and the deglaciation spike in pteropods and foraminifera. *Nature* **269**, 301 (1977).
87. B. A. A. Hoogakker *et al.*, Dynamics of North Atlantic Deep Water masses during the Holocene. *Paleoceanography* **26**, (2011).
88. W. S. Broecker, Abrupt climate change: causal constraints provided by the paleoclimate record. *Earth-Science Reviews* **51**, 137 (2000).
89. D. L. Lund, J. Lynch-Stieglitz, W. B. Curry, Gulf Stream density structure and transport during the past millennium. *Nature* **444**, 601 (2006).